

# The 2XMMi/SDSS Galaxy Cluster Survey

## II. The optically confirmed cluster sample and the $L_X - T$ relation<sup>\*</sup>

A. Takey<sup>1,2</sup>, A. Schwobe<sup>1</sup>, and G. Lamer<sup>1</sup>

<sup>1</sup> Leibniz-Institut für Astrophysik Potsdam (AIP), An der Sternwarte 16, 14482 Potsdam, Germany  
e-mail: atakey@aip.de

<sup>2</sup> National Research Institute of Astronomy and Geophysics (NRIAG), Helwan, Cairo, Egypt

Received ....; accepted ....

### ABSTRACT

**Aims.** We compile a sample of X-ray-selected galaxy groups and clusters from the XMM-Newton serendipitous source catalogue (2XMMi-DR3) with optical confirmation and redshift measurement from the Sloan Digital Sky Survey (SDSS). We present an analysis of the X-ray properties of this new sample with particular emphasis on the X-ray luminosity-temperature ( $L_X - T$ ) relation.

**Methods.** The X-ray cluster candidates were selected from the 2XMMi-DR3 catalogue in the footprint of the SDSS-DR7. We developed a finding algorithm to search for overdensities of galaxies at the positions of the X-ray cluster candidates in the photometric redshift space and to measure the redshifts of the clusters from the SDSS data. For optically confirmed clusters with good quality X-ray data we derived the X-ray flux, luminosity, and temperature from proper spectral fits, while the X-ray flux for clusters with low-quality X-ray data was obtained from the 2XMMi-DR3 catalogue.

**Results.** The detection algorithm provides the photometric redshift of 530 galaxy clusters. Of these, 310 clusters have a spectroscopic redshift for at least one member galaxy. About 75 percent of the optically confirmed cluster sample are newly discovered X-ray clusters. Moreover, 301 systems are known as optically selected clusters in the literature while the remainder are new discoveries in X-ray and optical bands. The optically confirmed cluster sample spans a wide redshift range 0.03-0.70 (median  $z=0.32$ ). In this paper, we present the catalogue of X-ray-selected galaxy groups and clusters from the 2XMMi/SDSS galaxy cluster survey. The catalogue has two subsamples: (i) a cluster sample comprising 345 objects with their X-ray spectroscopic temperature and flux from the spectral fitting, and (ii) a cluster sample consisting of 185 systems with their X-ray flux from the 2XMMi-DR3 catalogue, because their X-ray data are insufficient for spectral fitting. For each cluster, the catalogue also provides the X-ray bolometric luminosity and the cluster mass at  $R_{500}$  based on scaling relations and the position of the likely brightest cluster galaxy (BCG). The updated  $L_X - T$  relation of the current sample with X-ray spectroscopic parameters is presented. We found the slope of the  $L_X - T$  relation to be consistent with published ones. We see no evidence for evolution in the slope and intrinsic scatter of the  $L_X - T$  relation with redshift when excluding the low-luminosity groups.

**Key words.** X-rays: galaxies: clusters, galaxies: clusters: general, surveys, catalogs, techniques: photometric, techniques: spectroscopic

### 1. Introduction

Galaxy clusters are the largest known gravitationally bound objects; studying them is important for both an intrinsic understanding of their systems and an investigation of the large-scale structure of the Universe. The multi-component nature of galaxy clusters offers multiple observable signals across the electromagnetic spectrum (e.g. Sarazin 1988; Rosati et al. 2002). The hot, ionised intra-cluster medium (ICM) is investigated at X-ray wavelengths and using the Sunyaev-Zeldovich (SZ) effect (Sunyaev & Zeldovich 1972, 1980). The cluster galaxies are most effectively studied through optical and near-infrared (NIR) photometric and spectroscopic surveys. The statistical studies of galaxy clusters provide complementary and powerful constraints on the cosmological parameters (e.g. Voit 2005; Allen et al. 2011).

X-ray observations offer the most powerful technique for constructing cluster catalogues. The main advantages of the X-ray cluster surveys are their excellent purity and complete-

ness, and moreover, the X-ray observables are tightly correlated with mass (e.g. Reiprich & Böhringer 2002; Allen et al. 2011). Reliable measurements of cluster masses allow us to measure both the mass function (Böhringer et al. 2002) and the power spectrum (Schuecker et al. 2003), which directly probe the cosmological models.

At X-ray wavelengths, galaxy clusters are simply identified as X-ray luminous, continuous, spatially extended, extragalactic sources (Allen et al. 2011). Several X-ray cluster samples have been constructed from previous X-ray missions and have been used for a variety of astrophysical studies (e.g. Romer et al. 1994; Forman et al. 1978; Scharf et al. 1997; Vikhlinin et al. 1998; Böhringer et al. 2000; Borgani et al. 2001; Böhringer et al. 2004; Burenin et al. 2007). The current generation of X-ray satellites, XMM-Newton, Chandra, and Suzaku, provided follow-up observations of individual clusters that allowed a precise determination of their spatially resolved spectra (e.g. Vikhlinin et al. 2009; Pratt et al. 2010; Arnaud et al. 2010). Several other projects are being conducted to detect galaxy clusters from the observations of the XMM-Newton, Chandra, and the X-ray Telescope on board of the Swift satellite (e.g. Barkhouse et al.

<sup>\*</sup> Full Tables 1 and 2 are only available in electronic form at the CDS via anonymous ftp to cdsarc.u-strasbg.fr (130.79.128.5) or via <http://cdsweb.u-strasbg.fr/cgi-bin/qcat?J/A+A/.../...>

2006; Kolokotronis et al. 2006; Finoguenov et al. 2007, 2010; Adami et al. 2011; Fassbender et al. 2011; Takey et al. 2011; Mehrrens et al. 2012; Clerc et al. 2012; Tundo et al. 2012; de Hoon et al. 2013).

We have started a serendipitous search for galaxy clusters based on extended sources in the 2XMMi-DR3 catalogue, the second XMM-Newton source catalogue (Watson et al. 2009), in the footprint of the SDSS-DR7. The main aim of the survey is to construct a large catalogue of newly discovered X-ray-selected groups and clusters from XMM-Newton archival observations. The catalogue will allow us to investigate the evolution of X-ray scaling relations as well as the correlation between the X-ray and optical properties of the clusters.

The survey comprises 1180 X-ray-selected cluster candidates. A cross-correlation of these with recently published optically selected SDSS galaxy cluster catalogues yielded photometric redshifts for 275 objects. Of these, 175 clusters were published by Takey et al. (2011, paper I hereafter) together with their X-ray luminosity, temperature, and mass. The first cluster sample from the survey covers a wide range of redshifts from 0.09 to 0.61. We extended the relation between the X-ray bolometric luminosity at  $R_{500}$  (the radius at which the cluster mean density is 500 times the critical density of the Universe at the cluster redshift) and the X-ray temperature towards significantly lower luminosities than reported in the literature and found that the slope of the linear  $L_X - T$  relation was consistent with that for more luminous clusters.

In the present paper, we expand the optically confirmed sample from the survey by searching for the optical counterparts of cluster candidates that had been missed by previous cluster-finding algorithms and their members detected in the SDSS imaging (see paper I for a sample of X-ray and optically selected groups and clusters). We present the algorithm we used to identify the optical counterparts of the X-ray cluster candidates and to estimate the cluster redshifts using SDSS data. As a result, we present a catalogue of X-ray-selected galaxy groups and clusters (including the objects in paper I) from the ongoing 2XMMi/SDSS galaxy cluster survey. The catalogue provides the X-ray properties (such as temperature, flux, luminosity, and mass) and the cluster photometric redshift and, where available, the cluster spectroscopic redshift and the position of the likely brightest cluster galaxy (BCG) of the optically confirmed cluster sample.

The X-ray luminosity-temperature ( $L_X - T$ ) relation was investigated by several authors (e.g. Markevitch 1998; Pratt et al. 2009; Mittal et al. 2011; Eckmiller et al. 2011; Reichert et al. 2011; Takey et al. 2011; Maughan et al. 2012; Hilton et al. 2012). These studies showed that the observed  $L_X - T$  relation is much steeper than that predicted by self-similar evolution. This indicates that the ICM is heated by an additional source of energy, which is mainly active galactic nuclei (AGN) (Blanton et al. 2011). Including of AGN-feedback in cosmological evolution models indeed gives a better agreement between simulated and observed  $L_X - T$  under certain circumstances (Hilton et al. 2012). Here, we present an updated  $L_X - T$  relation based on the largest sample of X-ray-selected groups and clusters to date drawn from a single survey based on XMM-Newton observations. The sample spans a wide redshift range from 0.03 to 0.67.

The organisation of this paper is as follows: In Section 2, we describe the construction of the X-ray cluster candidate list and the optically confirmed cluster sample with their redshift estimates. In Section 3, we present the X-ray data reduction and analysis of the sample. In Section 4, the results and discussion

of the cluster sample is presented. We summarise our results in Section 5. The cosmological parameters  $\Omega_M = 0.3$ ,  $\Omega_\Lambda = 0.7$ , and  $H_0 = 70 \text{ km s}^{-1} \text{ Mpc}^{-1}$  were used throughout this paper.

## 2. Sample construction

We started our search based on the XMM-Newton serendipitous sources followed by searching for overdensities of galaxies in 3D space. In the following subsections, we present the strategy we followed to create the X-ray cluster candidate list. To derive the X-ray properties of these candidates, we needed to determine their redshift either from the X-ray data, which is only possible for the X-ray-brightest clusters, or from the optical data, which is the way we used in the current work. We also present the algorithm we used to detect the clusters in the optical band and to estimate their redshifts from the SDSS data. We compare the measured redshifts with the published values.

### 2.1. X-ray cluster candidates

The survey comprises X-ray cluster candidates selected as serendipitous sources from the 2XMMi-DR3 catalogue in the footprint of SDSS-DR7. The number of XMM-Newton fields that were used in constructing the 2XMMi-DR3 catalogue in the footprint of SDSS-DR7 at high galactic latitude  $|b| > 20^\circ$  is 1200 fields after excluding the multiple observations of the same field. We also excluded fields that were flagged as bad (the whole field) and unsuitable for source detection according to the manual flag given in the 2XMMi-DR3 catalogue. The total area of the fields included in our survey is  $210 \text{ deg}^2$ , taking into account the overlap areas among the fields.

The cluster candidate selection was based on X-ray-extended sources that passed the quality assessment during the construction of the catalogue by the XMM-Newton Survey Science Center (SSC). The extent parameter of each extended source in the 2XMMi-DR3 catalogue is determined by the SAS task `emldetect` by fitting a convolution of a  $\beta$  model ( $\beta=2/3$ ) and the instrument point spread function (PSF) to each input source. The source is classified as extended if the extent parameter varies between 6 to 80 arcsec and if the extent likelihood is higher than 4 (Watson et al. 2009).

The completeness of the 2XMMi-DR3 extended source catalogue is not easy to assess because the 2XMMi-DR3 catalogue was constructed from 4953 observations with different exposure times. The wide range of exposure times yields various flux limits. Mühlegger (2010) simulated two fields (LBQS and SCSA with exposure time 52 ks and 8.8 ks, respectively) in the XMM-Newton Distant Cluster project (XDCCP) to test the detection probability. They used a source detection technique that is similar to the one used in detecting the 2XMMi-DR3 sources. According to their simulations, the higher detection probability was achieved for clusters with intermediate core radii in the range of 15 to 25 arcsec. The probability decreases with decreasing photon counts and decreasing core radius ( $< 7$  arcsec) due to the difficulty to distinguish extended sources from point sources. The detection probability of sources with large core radii ( $> 75$  arcsec) and a low number of photons was low because these systems disappear in the background due to their low surface brightness. The detection probability decreases beyond the off-axis angle of 12 arcmin, caused by vignetting. Based on these results, clusters with low photon counts or large core radii might be missed in the 2XMMi-catalogue or might be listed with incorrect source parameters.

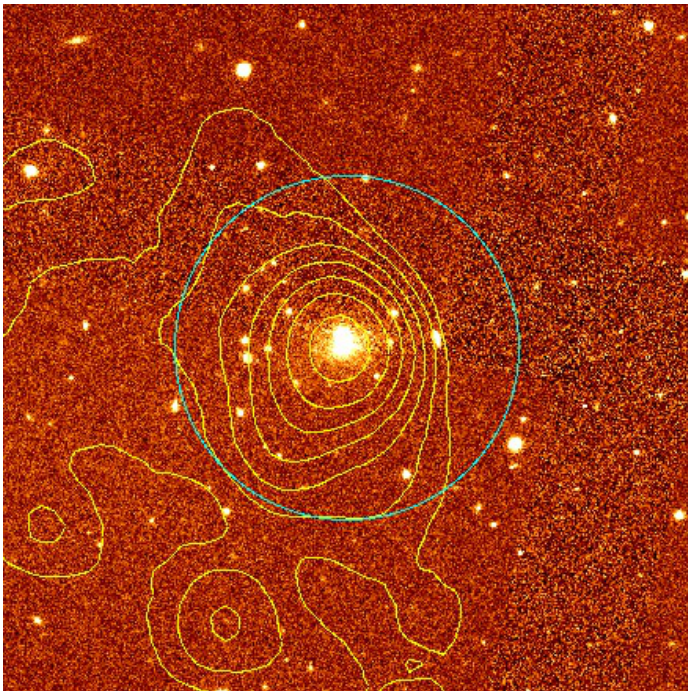


**Fig. 1.** X-ray-optical overlay of the example cluster 2XMM J102133.2+213752 at spectroscopic redshift = 0.1873. The X-ray flux contours (0.2 - 4.5 keV) are overlaid on a combined image from  $r$ ,  $i$ , and  $z$ -bands SDSS images. The plotted cyan circle has a radius of one arcmin around the X-ray emission peak. The field of view is  $4' \times 4'$  centred on the X-ray cluster position.

The selected extended sources were visually inspected by us in two steps to exclude possibly spurious detections. The first visual inspection was made using the X-ray images through the FLIX upper limit server<sup>1</sup>. The second one was made using the X-ray-optical overlays, where the X-ray flux contours were overlaid onto the co-added SDSS images in  $r$ ,  $i$ , and  $z$ -bands. The first inspection allowed us to remove the obviously spurious cases caused by point source confusion, X-ray artefacts, and locations near very bright sources. Extended sources were also rejected if they were found within another extended source or at the very edge of the CCDs. The second inspection enabled us to also remove the X-ray-extended sources corresponding to low-redshift galaxies. The resulting list includes 1180 X-ray cluster candidates with at least 80 net photon counts. More than 75 percent are new X-ray detections of galaxy groups and clusters.

Figure 1 shows the X-ray-optical overlay of a newly discovered galaxy cluster in X-ray and optical observations at redshift = 0.1873. This cluster has been serendipitously detected (at an off-axis angle of about 11 arcmins) in XMM-Newton EPIC observations of the galaxy NGC 3221. We use this cluster as an example to illustrate the main steps of estimating the cluster redshift and the X-ray analyses in the following sections.

## 2.2. Constructing the optically confirmed cluster sample

Various methods have been developed to define the cluster membership of galaxies from the data provided by the SDSS. They are based on different properties of the clusters and their galaxy members, for instance, using the cluster's red sequence, the E/S0 ridge-line (e.g. Koester et al. 2007; Hao et al. 2010), or an over-

density of galaxies in the photometric redshift space (Wen et al. 2009). Galaxy clusters are also identified by convolving the optical galaxy survey with a set of filters in position, magnitude, and redshift space based on modelling the cluster and field galaxy distributions (Szabo et al. 2011).

In paper I, we have optically confirmed about a quarter of the X-ray cluster candidates through cross-correlation with previously identified clusters in four optical cluster catalogues (Hao et al. 2010; Wen et al. 2009; Koester et al. 2007; Szabo et al. 2011). The remainder of the X-ray cluster candidates are either distant cluster candidates beyond the SDSS detection limits, that is,  $z \geq 0.6$ , which need follow-up imaging and spectroscopic confirmation, or there are overdensities of galaxies at the X-ray cluster positions that were not recognized by any previous optical cluster finders (see e.g. Figure 1). We therefore developed our own algorithm for clusters with members detected in the SDSS imaging to search for optical counterparts and determine their redshift from photometric redshifts in the SDSS database.

### 2.2.1. Estimation of the cluster redshifts

Because we have prior information about the cluster position, the position of the X-ray emission peak, we can use this information to simplify the cluster-finding procedure. We searched for an overdensity of galaxies around the X-ray position of the cluster candidates within a certain redshift interval. We created a galaxy sample for each X-ray cluster candidate by selecting all galaxies from the SDSS-DR8 in an area with a radius of 10 arcmin centred on the X-ray source position. This radius corresponds to a physical radius of 500 kpc at redshift 0.04, which is about our low-redshift limit.

The galaxies were selected from the galaxy view table in the SDSS-DR8, which contains the photometric parameters measured for resolved primary objects, classified as galaxies. The photometric redshifts and, where available, the spectroscopic redshifts of the galaxy sample were also selected from the Photoz and Specz tables, respectively, in the SDSS-DR8. The extracted parameters of the galaxy sample include the coordinates, the model magnitudes in  $r$ -band, the photometric redshifts, and, where available, the spectroscopic redshifts. Where galaxy spectroscopic redshifts were available, we used these instead of the photometric redshifts.

To clean the galaxy sample from faint objects or from galaxies with poor photometric measurements, we only used galaxies with  $m_r \leq 22$  mag and  $\Delta m_r < 0.5$  mag. The resulting galaxy sample still includes galaxies with large photometric redshift errors, which reach 100 percent in many cases. The photometric redshift errors of the galaxy sample with the applied magnitude cut are plotted against the photometric redshifts in Figure 2. To exclude low-redshift galaxies with significantly large relative photometric redshift errors as well as to keep high-redshift galaxies with moderately large relative errors that were acceptable, we decided to apply a relative photometric redshift error cut (< 50 percent) instead of using a fixed absolute error. The 50 percent relative error line is plotted in Figure 2.

The main idea of the finding algorithm is to identify the likely brightest cluster galaxy (BCG) among the galaxies with similar redshift within one arcmin from the X-ray centroid position and then search for an overdensity of surrounding member candidates. To confirm the X-ray cluster candidates optically and to measure their redshifts, we followed these steps:

<sup>1</sup> <http://www.ledas.ac.uk/flix/flix.html>

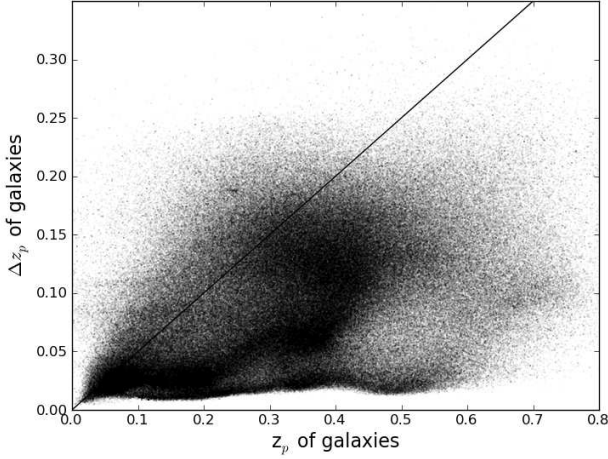


**Fig. 2.** Photometric redshift error,  $\Delta z_p$ , plotted against the photometric redshift,  $z_p$ , of the galaxy sample with  $m_r \leq 22$  mag and  $\Delta m_r < 0.5$  mag. The solid line indicates the 50 percent relative error of the photometric redshift of the galaxy sample.

1. We plotted the photometric redshift histogram of all galaxies within one arcmin from the X-ray position with  $m_r \leq 22$  mag,  $\Delta m_r < 0.5$  mag and the fractional error of the photometric redshift  $\Delta z_p/z_p < 0.5$ , as shown in Figure 3.
2. We computed a tentative photometric redshift of the cluster as the centre of the redshift bin in the main peak,  $z_{p,M}$ . To ensure that the distributions of the photometric redshifts of background galaxies did not produce this peak in the histogram, we selected 360 random positions in the SDSS sky coverage and counted the galaxies with the same magnitude and photometric redshift criteria as were used in the previous step within one arcmin from the field positions. We chose this large number of fields to obtain the average redshift distribution of background galaxies. Figure 4 shows the average distribution of the galaxy counts within these fields as a function of redshift. The distribution does not exceed 0.91 per redshift bin. It is unlikely that the background galaxies have a significant influence on the redshift determination. Therefore, we can neglect subtracting the background galaxies in the current step to compute a tentative cluster redshift.
3. We identified the BCG as the brightest galaxy of the galaxies within one arcmin around the X-ray position with a photometric redshift in the interval  $z_{p,M} \pm 0.04(1 + z_{p,M})$ . When the algorithm found multiple peaks in the redshift histogram, we selected the BCG candidate closest to the X-ray position. Wen et al. (2009) have shown that a redshift interval of  $\pm 0.04(1 + z_{p,M})$  comprises 80 percent of the clusters members. We assumed that our tentative redshift gives a less reliable but still robust estimate of cluster membership. The redshift of the likely BCG does not necessarily lie in the peak bin of the redshift histogram, but may be within one of the adjacent bins. Therefore, we initially allowed that the BCG candidate lies either in the central or in one of the adjacent redshift bins. We then chose as BCG the brightest galaxy in the bins nearest to the X-ray position.
4. To detect an overdensity of galaxies in 3D space, all galaxies within a radius of 560 kpc from the X-ray emission peak within the redshift interval  $z_{p,BCG} \pm 0.04(1 + z_{p,BCG})$  were considered as cluster member candidates,  $N(<560 \text{ kpc})$ . The redshift range used here is the same as that used by Wen et al.

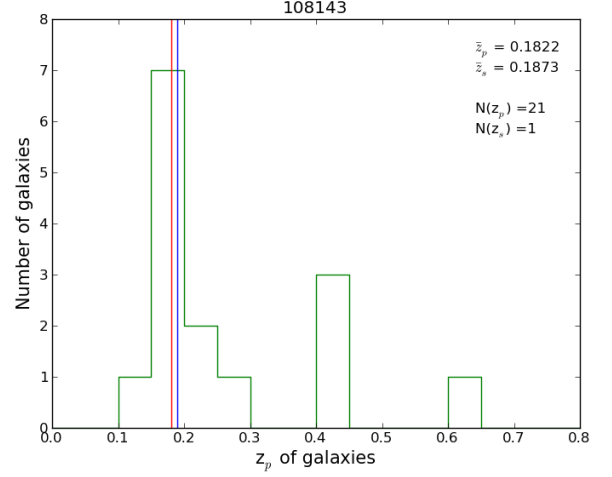


**Fig. 3.** Photometric redshift distribution of all galaxies within one arcmin from the X-ray centroid with  $m_r \leq 22$  mag,  $\Delta m_r < 0.5$  mag, and  $\Delta z_p/z_p < 0.5$ . The cluster photometric redshift (red line),  $\bar{z}_p$ , spectroscopic redshift (blue line),  $\bar{z}_s$ , and the cluster member candidates within 560 kpc with photometric redshift,  $N(z_p)$ , and spectroscopic redshift,  $N(z_s)$ , are listed in upper right corner.

(2009). Since the physical size of the cluster is not a priori known, we chose a radius of 560 kpc as the average of  $R_{500}$  from paper I. This radius is similar to the radius used by Wen et al. (2009) for detecting galaxy overdensity. These authors showed using Monte Carlo simulation tests that a radius of 500 kpc gives a high overdensity level and a low false detection rate. Because we are not computing the cluster richness in the current work, we did not subtract the background galaxies. The identified cluster member candidates were only used to compute the cluster redshift.

5. The cluster photometric redshift,  $\bar{z}_p$ , was finally determined as the weighted average of the photometric redshift of  $N(<560 \text{ kpc})$  with weights given as  $w_i = 1/(\Delta z_{p,i})^2$ . The redshift value for our example cluster is marked by the vertical red line in Figure 3. When there were available spectroscopic redshifts of  $N(<560 \text{ kpc})$ , the cluster spectroscopic redshift,  $\bar{z}_s$ , was the weighted average of the available spectroscopic redshifts, as indicated by the blue line in Figure 3. For the example cluster, only the BCG has a spectroscopic redshift. Figure 5 shows the sky distribution of the cluster member candidates within 560 kpc from the X-ray centroid; they are represented by red dots, and the field galaxies are represented by blue dots.
6. A cluster was considered detected when there were at least eight cluster member galaxies within 560 kpc and two members within one arcmin. When  $N(<560 \text{ kpc}) < 8$  but the estimated redshift was consistent with either an available redshift from the literature or spectroscopic redshift from the current algorithm, we also considered it detected cluster. The final decision to confirm the optical cluster detection was made by visual inspection of the SDSS colour image of the cluster field, which led to the exclusion of misidentified optical counterparts in a few cases. Figure 6 shows the SDSS colour image of the example cluster with a field of view  $4' \times 4'$  centred at the X-ray position.

Our procedure yielded 530 optically confirmed galaxy clusters with measured redshifts. We refer to this sample as the op-

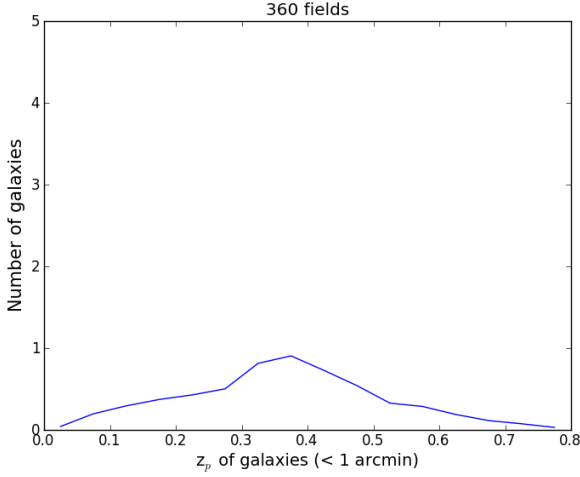


**Fig. 4.** Distribution of the mean galaxy counts, same distribution as Figure 3, within one arcmin from the positions of 360 random fields in the SDSS footprint with  $m_r \leq 22$  mag,  $\Delta m_r < 0.5$  mag, and  $\Delta z_p / z_p < 0.5$ .

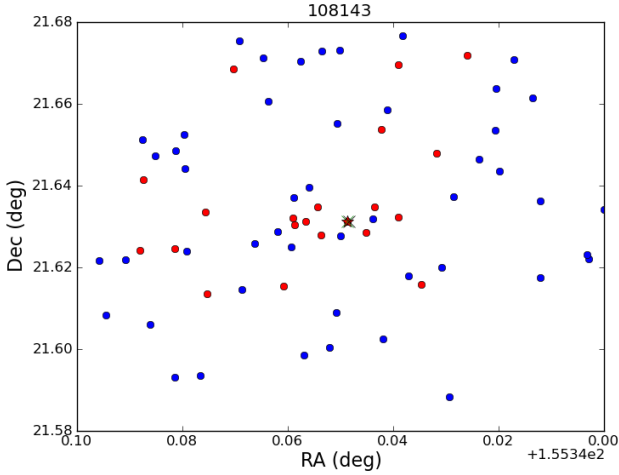


**Fig. 5.** Sky distribution of cluster galaxies (red dots) and field galaxies (blue dots) within 560 kpc from the X-ray position (black X marker). The BCG with an available spectroscopic redshift (marked by star) is located at the same place as the X-ray cluster position (green x marker).

tically confirmed cluster sample, which spans a wide redshift range from 0.03 to 0.70. About 60 percent of this sample are spectroscopically confirmed. Figure 7 shows the distribution of the number of cluster galaxies per cluster with spectroscopic redshifts. Figure 8 shows the distribution of the estimated photometric redshifts and, where available, spectroscopic redshifts of the optically confirmed cluster sample. The projected separation between the X-ray centres and the optical centres (chosen to be the BCGs positions) of the cluster sample is shown in Figure 9. The distribution has a median offset of 29 kpc, 86 percent of the BCGs are found within 150 kpc. The maximum projected separation between the BCGs and X-ray peaks is about 320 kpc. The reason for the small observed offset lies in the way of the sample construction, but the offset distribution seems to agree with the corresponding distribution derived for the maxBCG survey and ROSAT clusters (Rykoff et al. 2008).

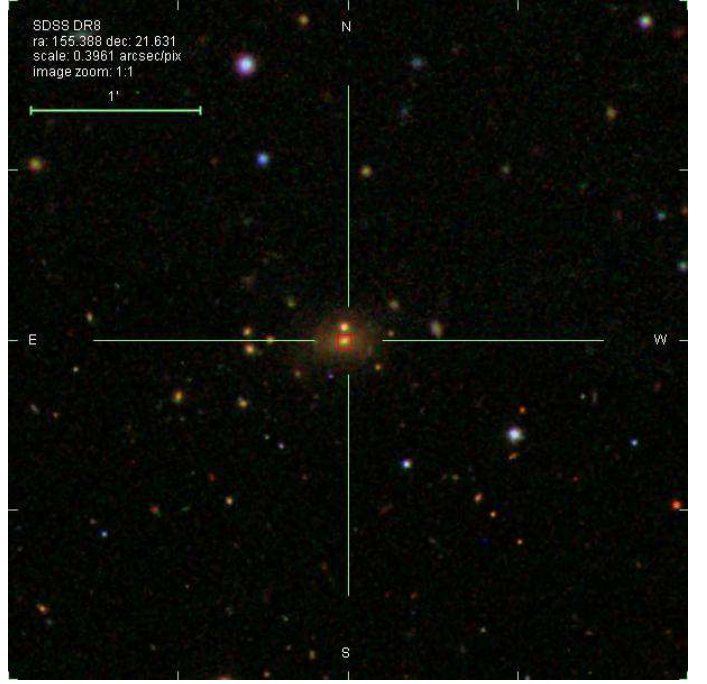


**Fig. 6.** SDSS colour image of the 2XMM J102133.2+213752 with a field of view of four arcmin a side centred on the X-ray peak position as indicated by the cross hair. The BCG with a spectroscopic redshift is marked by a square and is coincident with the X-ray position.

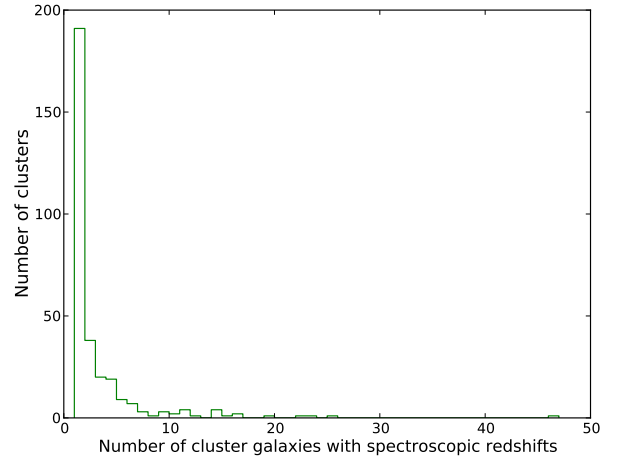


**Fig. 7.** Distribution of the number of cluster members with spectra of the spectroscopically confirmed clusters. The bin size of the histogram is one.

### 2.2.2. Redshift uncertainty and comparison with published redshifts

To assess the optical detection algorithm and the estimation of the cluster redshift, we queried the NASA Extragalactic Data base (NED) to search for published optical redshifts. The NED lists 301 objects including those from our paper I. Figure 10 shows the relation between our estimate of the redshifts,  $z_{pre}$ , and the published ones,  $z_{pub}$ . The clusters with available spectroscopic redshifts are represented by the green dots, the clusters with photometric redshifts only are represented by the blue dots.

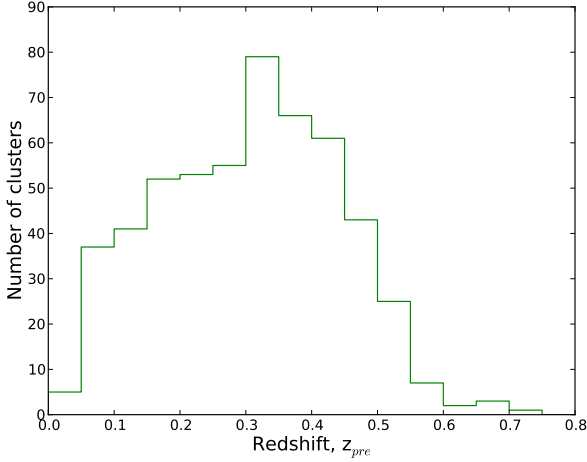


**Fig. 8.** Distribution of estimated photometric redshifts and, where available, the spectroscopic redshifts of the optically confirmed cluster sample.

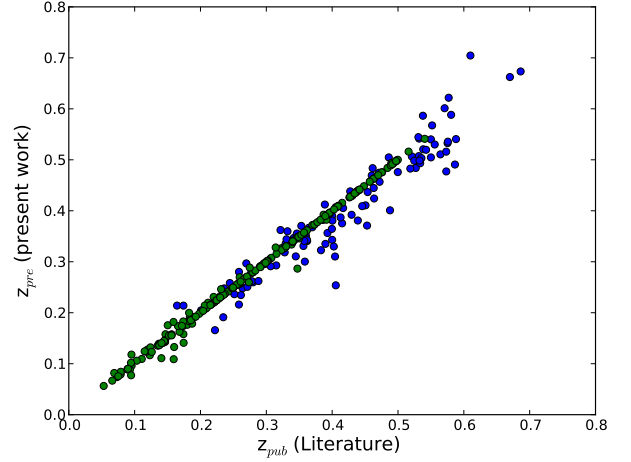


**Fig. 10.** Comparison between the estimated redshifts,  $z_{pre}$ , and the published ones,  $z_{pub}$ , of the optically confirmed cluster sample. The green dots represent the clusters with spectroscopic redshifts, while blue dots represent the clusters with photometric redshifts only.

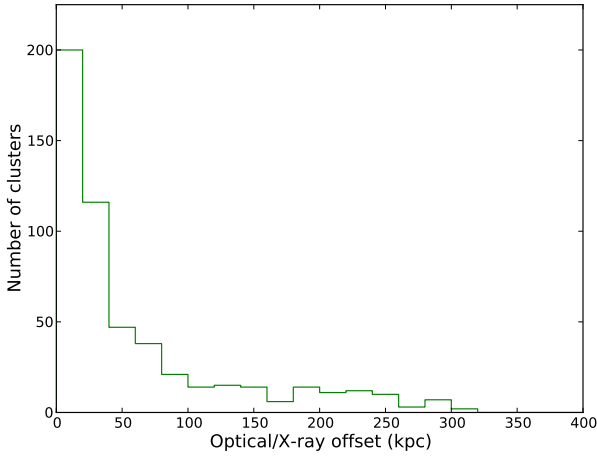


**Fig. 9.** Distribution of the linear separation between the likely BCG and the X-ray emission peak of the optically confirmed cluster sample.

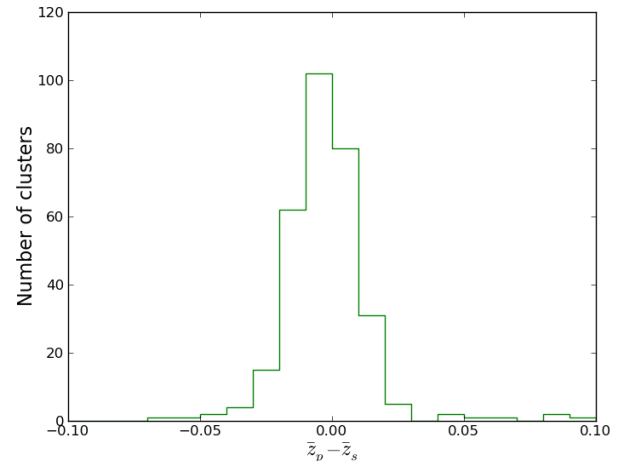


**Fig. 11.** Distribution of the differences between the photometric,  $\bar{z}_p$ , and spectroscopic,  $\bar{z}_s$ , redshifts of the optically confirmed cluster sample.

In general, the newly estimated redshifts agree very well with the published ones.

For clusters with a redshift difference  $|z_{pre} - z_{pub}| > 0.05$ , about 5 percent of the sample, we visually re-investigated the colour image (as in Figure 6) and the distribution on the sky of the identified cluster members (as in Figure 5). This led in all cases to a revision of the published redshifts, and we therefore regard the newly determined redshifts as more reliable than the published ones, which were based on optical search methods alone. We note that the redshifts used in paper I also needed to be revised for about 5 percent of the objects for the same reason.

Of the optically confirmed cluster sample, 310 galaxy clusters are spectroscopically confirmed with at least one member galaxy with spectroscopic redshift from the existing SDSS data (SDSS-DR8). To assess the accuracy of our weighted average photometric redshift,  $\bar{z}_p$ , we compared it with the weighted average spectroscopic redshift,  $\bar{z}_s$ . Figure 11 shows the distribution of the redshift differences,  $\bar{z}_p - \bar{z}_s$ , of the sample. The standard deviation of these redshift differences is 0.02, which roughly

indicates the accuracy of the estimated photometric redshifts. Therefore, we are confident about the reliability of the photometric redshift measurements.

### 3. X-ray data analysis

We used a similar procedure to that in paper I to reduce and analyse the X-ray data of the optically confirmed cluster sample. The raw XMM-Newton data were downloaded using the Archive InterOperability System (AIO), which provides access to the XMM-Newton Science Archive (XSA: Arviset et al. 2002). These data were reprocessed to generate the calibrated and filtered event lists for the EPIC (MOS1, MOS2, and PN) cameras with a recent version of the XMM-Newton Science Analysis Software (SAS11.0.1). To determine the source extraction radii with the highest signal-to-noise ratio (S/N), we created the radial profiles in the energy band [0.5-2.0] keV of each

camera as well as for EPIC. Then the S/N was calculated as a function of radius taking into account the background values as given in the 2XMMi catalogue.

The X-ray spectra of each cluster were generated from a region with the determined optimum extraction radius, which corresponded to the highest EPIC S/N. The spectral extraction from the optimal aperture was chosen to reduce the statistical uncertainty in the derived temperatures and luminosities from the spectral fits. The background spectra were extracted from a circular annulus around the cluster with inner and outer radii equaling two and three times the optimum radius, respectively. Other field sources embedded in the source and background regions of the cluster were removed.

The extracted spectra were binned to one count per bin. Spectra for each cluster were simultaneously fitted in XSPEC (Arnaud 1996, version 12.7.0) with a single-temperature optically thin thermal plasma model modified by galactic absorption of neutral matter, TBabs \* MEKAL in XSPEC terminology (Mewe et al. 1986; Wilms et al. 2000). The temperature and the normalisation of the plasma model were allowed to vary while the abundance was fixed at  $0.4 Z_{\odot}$ . The hydrogen absorbing column density,  $nH$ , was derived from the Leiden/Argentine/Bonn (LAB) survey (Kalberla et al. 2005) and was fixed to this value. The spectral fit was performed using the Cash statistics with one count per bin, a recommended strategy for sources with low photon counts (e.g. Krumpke et al. 2008).

To avoid a conversion of the fit to a local minimum of the fitting statistics, we ran series of fits stepping the temperature from 0.1 to 15 keV with a step size = 0.05 using the `steppar` command within XSPEC. We note that when the model spectrum is interpolated from a pre-calculated table, the cluster temperatures in some cases tend to converge exactly at the temperature grid points of the model table. Therefore, we ran the MEKAL code with the option of calculating the model spectrum for each temperature during the fitting and stepping process.

The spectral fitting provided us with the X-ray temperatures, fluxes in [0.5-2.0] keV, and luminosities in the rest frame energy band [0.5-2.0] keV and their errors. The errors of the X-ray temperatures, fluxes, and luminosities represent the 68 percent confidence range. The bolometric X-ray luminosity over the rest frame energy range (0.1 to 50.0) keV was determined from the dummy response matrices based on the best-fitting model parameters. The fractional error in the bolometric luminosity was assumed to be the same as the fractional error of the luminosity in the given energy band. To confirm that this assumption is valid, we varied the temperatures by  $\pm 1 \sigma$  in a few cases. We found the measured band luminosities to be within their errors.

We accepted the X-ray parameters (temperature, flux, luminosity) of a cluster if the relative errors of both the temperature and luminosity were smaller than 50 percent. A final check was made to ensure that neither the source nor the background region were affected by detector artefacts and/or astronomical objects. We also visually screened spectral fits applied to the data and rejected poor spectral fits.

Finally, the derived bolometric luminosities were used to estimate the cluster luminosities and masses at  $R_{500}$  through an iterative method, as briefly described below and as discussed in more detail in paper I.

## 4. Results and discussion

We were able to derive reliable X-ray parameters from spectral fits for 345 systems of the optically confirmed cluster sample. In

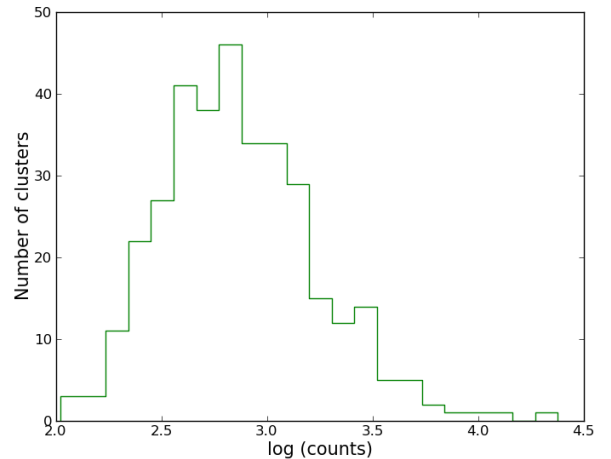


**Fig. 12.** Distribution of the aperture net EPIC photon counts in [0.5-2.0] keV derived from the spectral fitting for the cluster sample with X-ray spectroscopic parameters.

the next subsections, we compare our new results with the common clusters from (a) the XMM Cluster Survey (Mehrtens et al. 2012), (b) the MCXC catalogue (Piffaretti et al. 2011), and (c) the paper I sample. We then proceed to derive an updated  $L_X - T$  relation based on this new sample. For the remaining 185 clusters of the optically confirmed sample without proper spectral fits, we used the X-ray flux as given in the 2XMMi-DR3 catalogue to estimate the luminosity and mass. We finally present the X-ray luminosity-redshift distribution of the whole optically confirmed cluster sample.

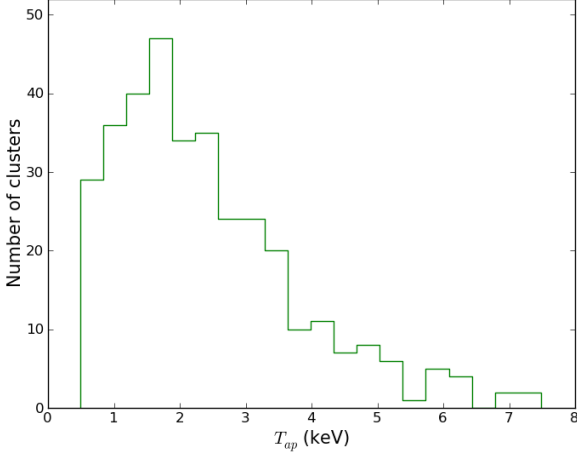
### 4.1. Cluster sample with reliable X-ray parameters from the spectral fits

Figure 12 shows the distribution of the net EPIC photon counts in the energy interval [0.5-2.0] keV for clusters that could be fitted successfully. It shows that 87 percent of our clusters have more than 300 source photons. In some cases a successful spectral fit could be achieved with just a few more than 100 photons by combining clean X-ray data and previous knowledge of the cluster redshift. Our new sample has a wide range of temperatures from 0.5 to 7.5 keV, which is shown in Figure 13. The average relative errors of the temperatures and luminosities are 0.20 and 0.06, respectively.

We followed an iterative method (see paper I) to compute the physical parameters for each cluster. The estimated aperture X-ray bolometric luminosity and its error, optimal extraction radius, and the redshift were used as input to determine the radius  $R_{500}$ , the X-ray bolometric luminosity within  $R_{500}$ ,  $L_{500}$ , and the cluster mass at  $R_{500}$ ,  $M_{500}$ . The main idea of the iterative method is to extrapolate the aperture bolometric flux to the bolometric flux at  $R_{500}$  based on a  $\beta$  model of the form

$$S(r) = S(0) \left[ 1 + \left( \frac{r}{r_c} \right)^2 \right]^{-3\beta+1/2}, \quad (1)$$

where  $\beta$  and core radius,  $r_c$ , depend on temperature (see Eq. 4 and 5 in paper I). The correction factor of the flux is used to extrapolate the aperture bolometric luminosity to the bolometric  $L_{500}$ . Finally,  $M_{500}$  is computed based on the  $L_{500} - M_{500}$  relation from Pratt et al. (2009). The error budget of the estimated  $L_{500}$



**Fig. 13.** X-ray spectroscopic temperature distribution of the cluster sample with reliable X-ray parameters from the spectral fit.

and  $M_{500}$  includes the errors of the input parameters, the intrinsic scatter in the  $L_X - T$  and  $L_X - M$  relations, and the propagated errors of their slopes and the intercepts. The median correction factor between the extrapolated bolometric luminosity to  $R_{500}$  and the aperture bolometric luminosity,  $L_{500}/L_{bol}$ , was 1.7.

Table 1, available in full form at the CDS, represents the first ten entries of the X-ray-selected cluster sample with a total of 345 rows. For each cluster the catalogue lists the cluster identification number (detection id, detid) and its name (IAUNAME) in (cols. [1] and [2]), the right ascension and declination of X-ray emission in equinox J2000.0 (cols. [3] and [4]), the XMM-Newton observation id (obsid) (col. [5]), the optical redshift (col. [6]), the scale at the cluster redshift in kpc'' (col. [7]), the aperture and  $R_{500}$  radii in kpc (cols. [8] and [9]), the cluster aperture X-ray temperature  $T_{ap}$  and its positive and negative errors in keV (cols. [10], [11] and [12], respectively), the aperture X-ray flux  $F_{ap}$  [0.5-2.0] keV and its positive and negative errors in units of  $10^{-14}$  erg cm $^{-2}$  s $^{-1}$  (cols. [13], [14] and [15], respectively), the aperture X-ray luminosity  $L_{ap}$  [0.5-2.0] keV and its positive and negative errors in units of  $10^{42}$  erg s $^{-1}$  (cols. [16], [17] and [18], respectively), the cluster bolometric luminosity  $L_{500}$  and its error in units of  $10^{42}$  erg s $^{-1}$  (cols. [19] and [20]), the cluster mass  $M_{500}$  and its error in units of  $10^{13}$   $M_{\odot}$  (cols. [21] and [22]), the Galactic HI column in units  $10^{22}$  cm $^{-2}$  (col. [23]), the objid of the likely BCG in the SDSS-DR8 (col. [24]), the BCG right ascension and declination in equinox J2000.0 (cols. [25] and [26]), the estimated photometric and, where available, the spectroscopic redshift of the cluster (col. [27] and col. [28]), the number of cluster members within 560 kpc with available spectroscopic redshifts that were used to compute the cluster spectroscopic redshift, (col. [29]), the redshift type (col. [30]), the linear offset between the cluster X-ray position and the BCG position (col. [31]), and the NED name and its references (col. [32] and col. [33]).

#### 4.2. Cluster sample with X-ray flux from the 2XMMi-DR3 catalogue

For clusters with insufficient X-ray data to perform a proper spectral fit, we estimated the X-ray parameters based on the EPIC flux and its error in 0.5-2.0 keV as given in the 2XMMi-DR3 catalogue. The catalogue provides aperture-corrected

fluxes that were calculated by the SAS tasks `emldetect`. For the individual cameras, individual-band fluxes were calculated from the respective band count rate using the filter- and camera-dependent energy conversion factors corrected for the dead time from the read-out phase. The EPIC flux in each band was estimated as the mean of the band-specific detections in all cameras weighted by their errors (Watson et al. 2009). Here we used the combined EPIC flux in band 2 (0.5 - 1.0 keV) and band 3 (1.0 - 2.0 keV) and its propagated error,  $F_{cat}$  in [0.5-2.0] keV.

Figure 14 shows the relation between the flux given in the 2XMMi-DR3 catalogue and the aperture flux determined by us for the 345 clusters with reliable X-ray parameters from the spectral fits. It shows a linear relation between the two flux measurements except for some outliers (about 5 percent), which we found to be contaminated by point sources in the 2XMMi-DR3 catalogue. In general terms, the catalogued flux is higher than the aperture flux because the former was computed for the integrated  $\beta$ -model.

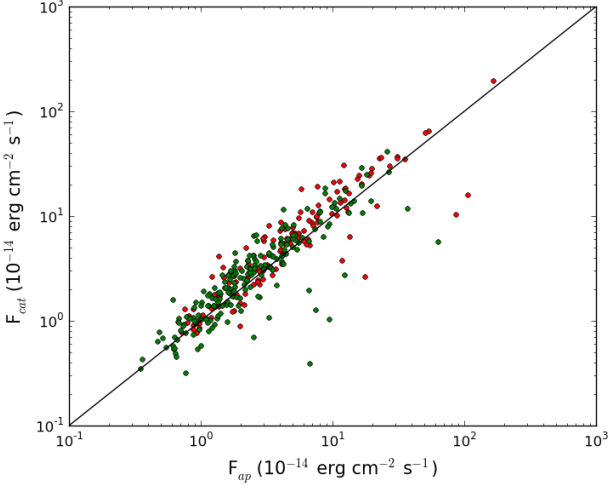
Figure 15 shows the relation between the aperture bolometric luminosities,  $L_{ap,bol}$ , and  $L_{cat,0.5-2.0}$  of the cluster sample with X-ray spectroscopic parameters, where  $L_{cat,0.5-2.0}$  is based on  $F_{cat}$  in [0.5-2.0] keV. Generally, there is a linear relation between the two luminosities except for 12 outliers with  $L_{ap,bol}/L_{cat,0.5-2.0} > 2$ . Ignoring these outliers, we performed a linear regression between their logarithms to convert  $L_{cat,0.5-2.0}$  to  $L_{ap,bol}$  for the 185 clusters without proper spectral fit. The best-fit linear relation derived using the BCES orthogonal regression method (Akritas & Bershady 1996) is represented by the dashed line in Figure 15 and is given by Eq. 2,

$$\log(L_{ap,bol}) = 0.07 + 1.10 \log(L_{cat,0.5-2.0}). \quad (2)$$

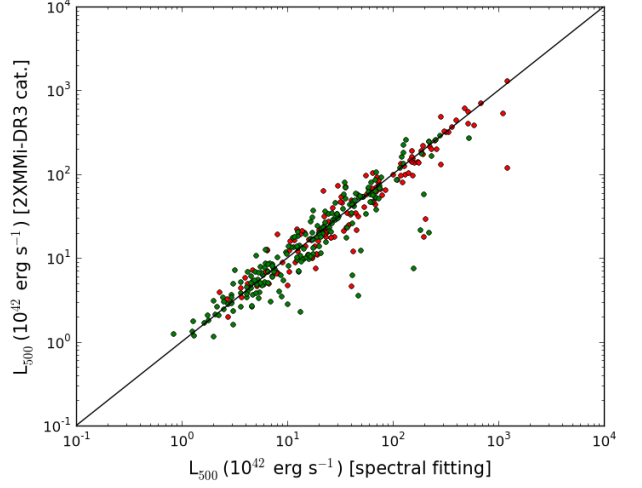
Using the iterative method described above, we computed the bolometric  $L_{500}$  per cluster with the redshift, aperture radius  $R_{ap}$  and aperture bolometric luminosity  $L_{ap,bol}$  as input. The aperture radius used here is still the radius that corresponds to the highest EPIC S/N, see Section 3. We finally determined for each cluster  $R_{500}$ ,  $M_{500}$ , and  $T_{500}$  and the corresponding errors using the extrapolated values for  $L_{500}$ . From the comparison between the bolometric  $L_{500}$  based on the catalogue flux and the bolometric  $L_{500}$  based on the spectroscopic flux, there is no obvious systematic difference between the two luminosities, as shown in Figure 16. Therefore, the conversion from  $L_{cat,0.5-2.0}$  to  $L_{ap,bol}$  and the iterative procedure are acceptable.

Table 2, a full version of which is provided at the CDS, represents the first 10 entries of the X-ray-selected cluster sample with X-ray parameters based on the given flux in the 2XMMi-DR3 catalogue, comprising 185 clusters. For each cluster, the catalogue provides the cluster identification number (detection id, detid) and its name (IAUNAME) in (cols. [1] and [2]), the right ascension and declination of X-ray emission in equinox J2000.0 (cols. [3] and [4]), the XMM-Newton observation id (obsid) (col. [5]), the optical redshift (col. [6]), the scale at the cluster redshift in kpc'' (col. [7]), the  $R_{500}$  in kpc (col. [8]), the 2XMMi-DR3 X-ray flux  $F_{cat}$  [0.5-2.0] keV and its error in units of  $10^{-14}$  erg cm $^{-2}$  s $^{-1}$  (cols. [9], and [10]), the estimated X-ray luminosity  $L_{cat}$  [0.5-2.0] keV and its error in units of  $10^{42}$  erg s $^{-1}$  (cols. [11], and [12]), the cluster bolometric luminosity  $L_{500}$  and its error in units of  $10^{42}$  erg s $^{-1}$  (cols. [13] and [14]), the cluster mass  $M_{500}$  and its error in units of  $10^{13}$   $M_{\odot}$  (cols. [15] and [16]), the  $T_{500}$  and its error in units of keV (cols. [17] and [18]), the objid of the likely BCG in SDSS-DR8 (col. [19]), the BCG right ascension and declination in equinox J2000.0 (cols. [20] and [21]), the estimated photometric and, where available, the spectroscopic redshift of the cluster (col. [22] and col. [23]), the





**Fig. 14.** Cluster flux,  $F_{cat}$ , in 0.5-2.0 keV from the 2XMMi-DR3 catalogue plotted against the cluster flux,  $F_{ap}$ , in 0.5-2.0 keV from the best-fitting model parameters for the cluster sample with spectroscopic parameters. The red dots represent the first cluster sample from paper I, while the green dots represent the extended sample with reliable X-ray parameters.



**Fig. 16.** Comparison between the measured bolometric luminosity  $L_{500}$  based on the flux given in the 2XMMi-DR3 catalogue and the bolometric  $L_{500}$  based on the spectral fit flux for the first (red dots) and extended (green dots) cluster sample with X-ray spectroscopic parameters from the survey. The solid line shows the one-to-one relationship.

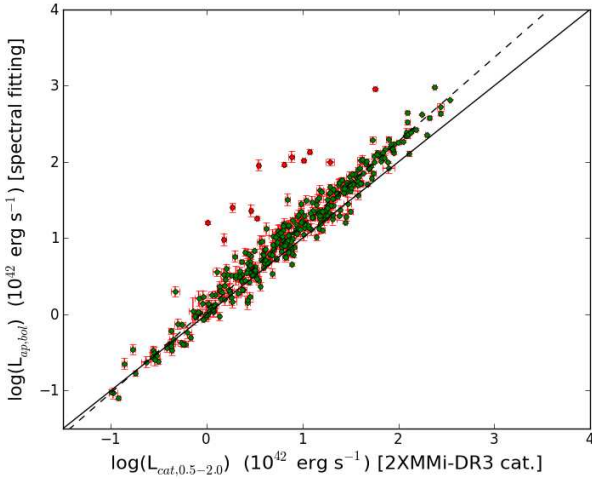


**Fig. 15.** Aperture bolometric luminosities,  $L_{ap,bol}$ , plotted against the 2XMMi-DR3 catalogue luminosities,  $L_{cat,0.5-2.0}$ , of the cluster sample with reliable parameters from the spectral fits. The one-to-one relationship is represented by the solid line. The dashed line represents the best-fit using the BCES orthogonal regression method after excluding 12 outliers that are represented by red dots.

number of cluster members within 560 kpc with available spectroscopic redshifts that were used to compute the cluster spectroscopic redshift, (col. [24]), the redshift type (col. [25]), the linear offset between the cluster X-ray position and the BCG position (col. [26]), and the NED name and its references (col. [27] and col. [28]).

#### 4.3. Analysis of the cluster sample with reliable X-ray parameters

We present a comparison of the measured parameters (temperatures, luminosities, and masses) of the cluster sample (345 sys-

tems) that have reliable X-ray parameters from the spectral fits with the values available in the literature.

##### 4.3.1. Comparison with the XCS sample

The largest published catalogue of X-ray clusters so far, based on the entire XMM-Newton archive, was compiled by the XMM Cluster Survey team (XCS, Romer et al. 2001; Lloyd-Davies et al. 2011; Mehrrens et al. 2012). The catalogue consists of 503 optically confirmed clusters. Of these, 463 systems have redshifts in the range 0.05 to 1.46. The X-ray temperatures were measured for 401 clusters. We cross-matched our cluster sample and the XCS sample with available temperature measurements within a matching radius of 30 arcsec, which yielded 114 common clusters. About half of the common sample was previously published by us in paper I. The standard deviation of the redshift difference ( $z_{XCS} - z_{pre}$ ) is 0.027 and is thus of about the photometric redshift accuracy. There is no systematic deviation for instance as a function of redshift, as shown in Figure 17.

Even though we extracted the cluster spectra from a different aperture than the aperture used in the XCS project and used a different spectral fitting procedure, the temperature measurement in general agrees. Figure 18 shows the comparison of the measured temperatures from the two projects. We plot the symmetric errors of each temperature as the average of the positive and negative errors. Our procedure reveals a slightly smaller temperature uncertainty than derived in the XCS, with a median  $\Delta T_{pre} / \Delta T_{XCS} = 0.84$ . The differences between the two temperature measurements have a mean of 0.02 keV and a standard deviation of 0.93 keV that is similar to the standard deviation, 0.82 keV, of the error measurements in temperatures of the XCS sample.

In the XCS project, the cluster luminosity  $L_{500}$  was calculated by using an analytical function of the  $\beta$  model fitted to the surface brightness profile. The same profile was used to determine a scaling factor between the aperture luminosity and  $L_{500}$  (Lloyd-Davies et al. 2011). Our procedure of the extrapolation

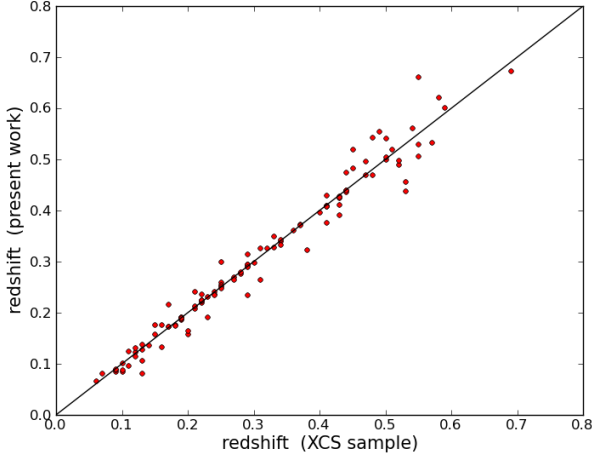


**Fig. 17.** Comparison of the estimated redshifts of the common sample between the XCS catalogue and our sample with X-ray spectroscopic parameters. The solid line in the figure indicates the unity line.

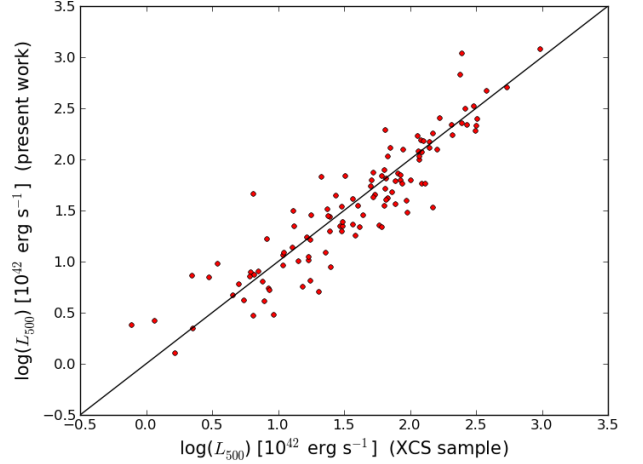


**Fig. 19.** Comparison between the bolometric luminosities,  $L_{500}$ , from the present work and the corresponding ones from the XCS sample. The solid line shows the one-to-one relationship.

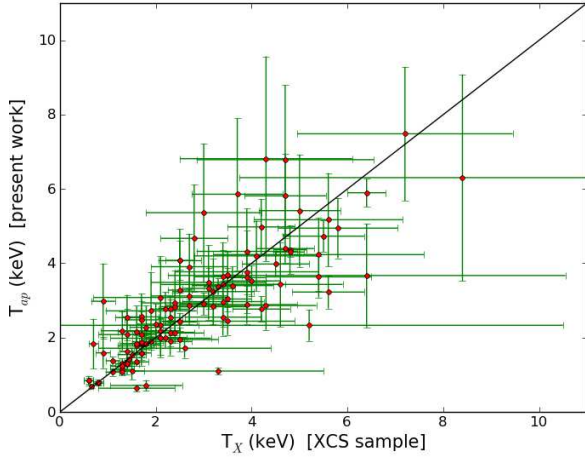


**Fig. 18.** Comparison of measured temperatures between  $T_{ap}$  in our sample and  $T_X$  in XCS sample. The solid line shows the one-to-one relationship. The errors are the average errors of positive and negative errors, which are provided by the spectral-fitting.

is described above and is discussed in more detail in paper I. We found a good agreement between both determinations of  $L_{500}$ , as shown in Figure 19. The ratio between the current luminosity measurements to that of the XCS has a median of 0.93.

#### 4.3.2. Comparison with the MCXC sample

The MCXC catalogue, a meta-catalogue of X-ray-detected galaxy clusters, is compiled from published ROSAT All Sky Survey-based and serendipitous cluster catalogues (Piffaretti et al. 2011). The catalogue comprises 1743 clusters that span a wide redshift range up to 1.3. For each cluster the catalogue lists redshift, luminosity  $L_{500}$  in the 0.1-2.4 keV band, total mass  $M_{500}$ , and radius  $R_{500}$ . Within a cross-matching radius of 30 arcsec there are only 23 common clusters. The small overlap is mainly due to our small survey

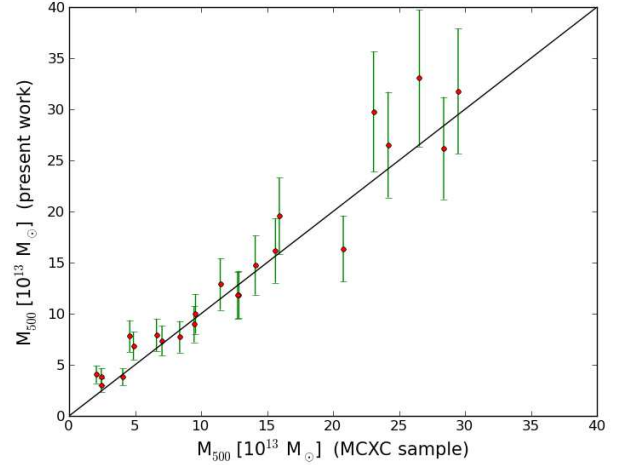


**Fig. 20.** Comparison of our sample mass estimates within  $R_{500}$  with the estimated values from the MCXC catalogue. The solid line represents the one-to-one relationship.

area and our strategy of investigating serendipitous clusters only, not cluster targets.

We compare the masses of the common sample in Figure 20 and find consistent results. This comparison makes sure that our mass measurements are reliable and not affected by any systematic bias. We also find consistency between the redshifts used in both catalogues.

#### 4.3.3. Comparison with the sample from paper I

Because we developed an algorithm for estimating the redshifts of the X-ray cluster candidates, the redshifts of the first cluster sample from the survey, paper I, were revised, as discussed in Section 2. We also revised the X-ray spectroscopic parameters for the first cluster sample. The sample in common between the current sample with reliable X-ray parameters and the first cluster sample consists of 141 systems. The remaining 34 clusters from paper I did not pass the quality criterion applied in the present work. These missed clusters are nevertheless included in

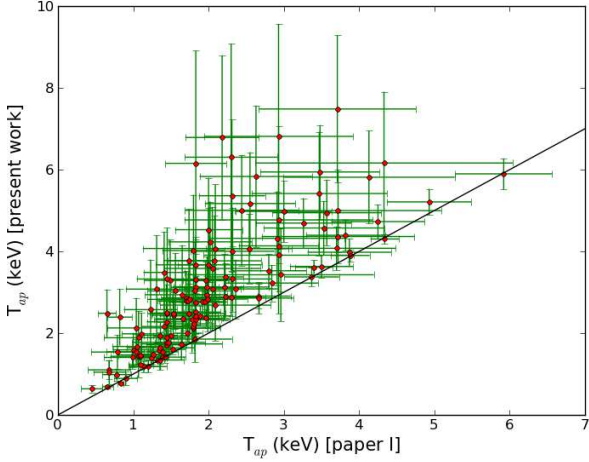


**Fig. 21.** Current X-ray aperture temperature estimates plotted against the corresponding ones of the first cluster sample from paper I. To facilitate the comparison, we plot the unity line.

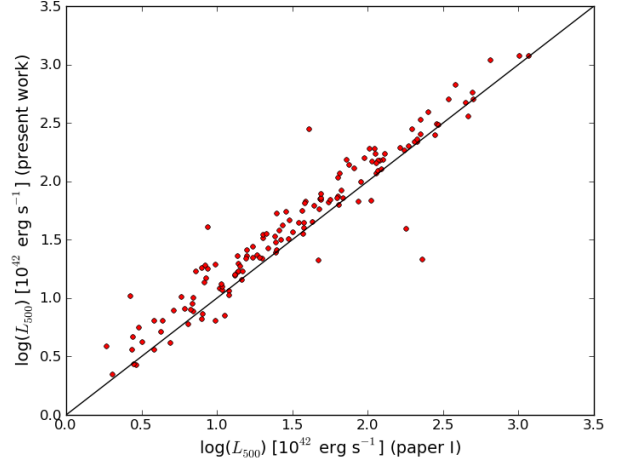


**Fig. 22.** Comparison between the bolometric luminosities,  $L_{500}$ , from the present work and the corresponding ones from paper I. The solid line shows the one-to-one relationship.

the published cluster catalogue from this paper with less reliable parameters (see above).

We found a systematic bias of the temperature measurements of the sample in paper I and the current sample (Figure 21). When investigating possible reasons for the discrepancy we realized that the X-ray data in Paper I were analysed in an inappropriate manner. The X-ray spectra were not grouped and binned before we applied a spectral model. This led to a systematic shift towards too low values of many of the derived temperatures determined in paper I.

As a consequence, the luminosities were biased towards lower values (Figure 22) by a factor of 20 percent. Revised redshifts and in some cases revised spectral extraction regions led to a few outliers in that figure.

We also presented in paper I the  $L_X - T$  of the first cluster sample, which we now regard as affected by the underestimated X-ray temperatures. We are confident through several sanity checks that our updated temperatures and luminosities are reliable, and we re-determine the  $L_X - T$  relation based on the much enlarged and more reliable sample in the next subsection.

#### 4.4. $L_X - T$ relation of the cluster sample with reliable X-ray parameters

Based on the cluster sample with X-ray spectroscopic parameters, we investigate the  $L_X - T$  relation as well as the evolution of its slope and intrinsic scatter as presented in the following subsections.

##### 4.4.1. $L_X - T$ relation of the full sample

The bolometric luminosities  $L_{500}$  and the aperture temperatures  $T_{ap}$  based on X-ray spectral fits were used to investigate the  $L_{500} - T_{ap}$  relation for the cluster sample with reliable X-ray parameters. We note that we were unable to attempt to excise the cores in most cases of the cluster sample because of the low resolution of the X-ray optics of the XMM-Newton telescopes, short exposure times, and the very large distance of most of our clusters. This caveat needs to be made when comparing our results with those in the literature, which are partly based on nearby clusters with Chandra follow-up.

Figure 23 shows the relation between the measured X-ray bolometric luminosity,  $L_{500}$ , modified with the evolution parameter for self-similar evolution and the X-ray aperture temperature,  $T_{ap}$ . We used the BCES orthogonal regression method (Akritas & Bershady 1996) to derive the best-fit linear relation between the logarithms of  $L_{500}$  and  $T_{ap}$  taking into account their errors as well as the intrinsic scatter. The best fit is shown in Figure 23 and is given by Eq. 3,

$$\log(h(z)^{-1} L_{500}) = (44.39 \pm 0.06) + (2.80 \pm 0.12) \log(T_{ap}/5), \quad (3)$$

where  $h(z)$  is the Hubble constant normalised to its present-day value,  $h(z) = [\Omega_M(1+z)^3 + \Omega_\Lambda]^{1/2}$ ,  $L_{500}$  in  $\text{erg s}^{-1}$ , and  $T_{ap}$  in keV. By an analysis of objects in common between our list and that of the XCS we have shown that our  $T_{ap}$  and  $L_{500}$  agree well with  $T_X$  and  $L_{500}$  of the XCS sample. Not unexpectedly, the slopes and intercepts of the corresponding  $L_X - T$  relations agree with each other within 1-2  $\sigma$  (see subsection 4.4.2).

Relations between the luminosity and the temperature,  $L_{500} - T_{500}$ , were published for the REXCESS and HIFLUGCS sample (Pratt et al. 2009; Mittal et al. 2011). The REXCESS sample comprises 31 nearby ( $z < 0.2$ ) galaxy clusters with a temperature range from 2 to 9 keV that have been observed with the XMM-Newton. The HIFLUGCS sample comprises the 64 brightest galaxy clusters in the sky with  $kT \geq 1$  keV and  $z \leq 0.2$ , with high-quality Chandra data. In both samples the core emission could be excised but  $L_X - T$  were published for the non-excised data as well. The REXCESS team used a fitting procedure similar to ours, the HIFLUGCS sample was fitted with a BCES-bisector routine.

The present slope of the relation in Eq. (3),  $2.80 \pm 0.12$ , is slightly lower than that from the REXCESS sample,  $3.35 \pm 0.32$ , but is still within  $1.8\sigma$ . We also found that the present slope agrees with the slope given by Mittal et al. (2011),  $2.94 \pm 0.16$ .

The current cluster sample includes groups with much lower luminosity than REXCESS and HIFLUGCS, which might influence the slope of the  $L_X - T$  relation. If we exclude systems with luminosities  $L_{500} < 5 \times 10^{42} \text{ erg s}^{-1}$ , the slope of the relation becomes  $3.07 \pm 0.19$ , which agrees much better with the published ones for the REXCESS, HIFLUGCS, and XCS samples. The normalisation of the relation,  $44.46 \pm 0.07$ , is still much lower

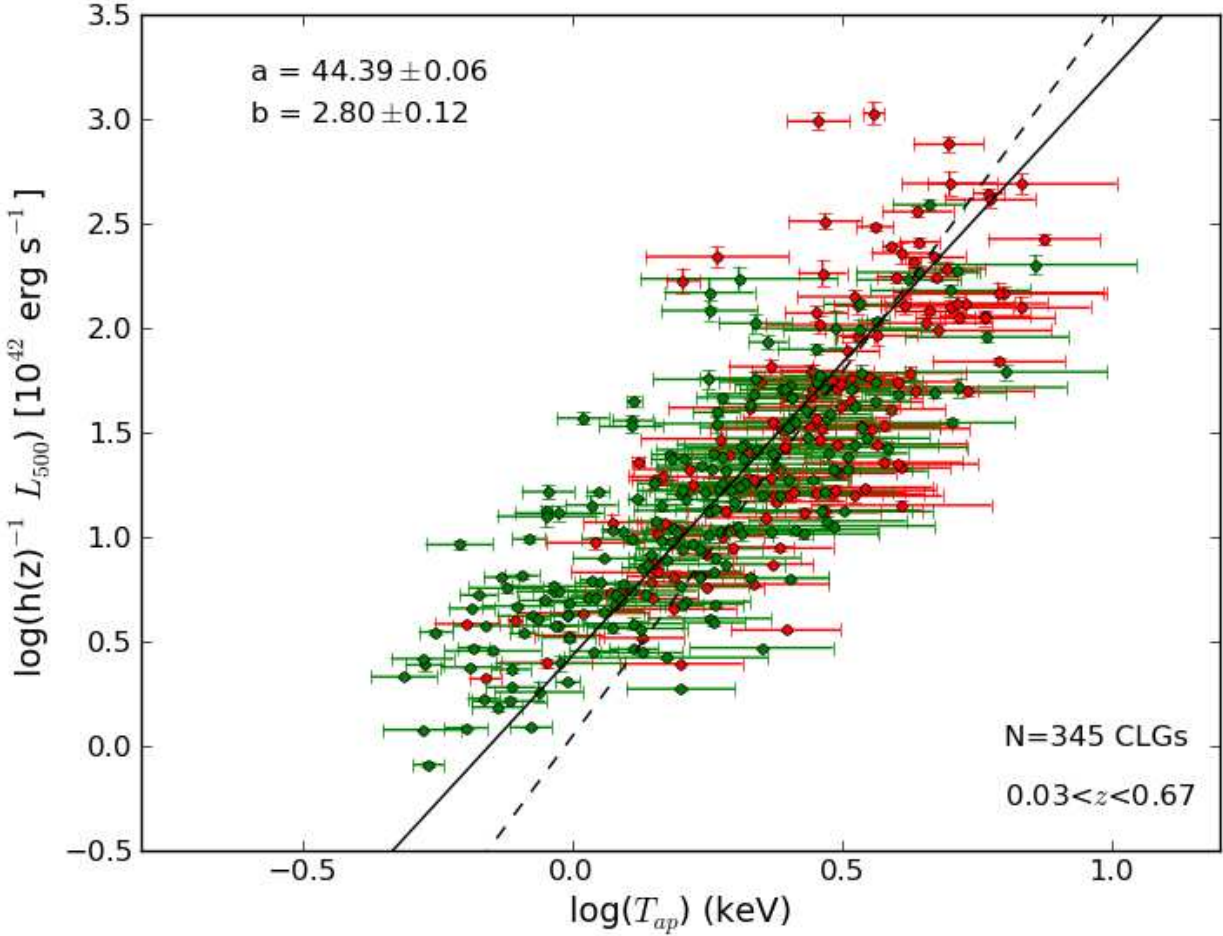


**Fig. 23.** X-ray bolometric luminosity,  $L_{500}$ , plotted against aperture X-ray spectroscopic temperature,  $T_{ap}$ , for the first (red dots) and expanding (green dots) cluster sample with reliable X-ray parameters. The solid line is the fit to both samples using the BCES orthogonal regression. The intercept,  $a$ , and the slope,  $b$ , of the fitted line are written in the upper left corner of the figure, while the sample number,  $N$ , and its redshift range are written in the lower right corner. The dashed line represents the relation fit of the first cluster sample using the current parameter measurements.

than that of the REXCESS sample,  $44.85 \pm 0.06$ . This is because a much wider temperature range is covered by the current large sample, in addition to establishing the current relation based on aperture temperatures that are in general slightly higher than the temperatures at  $R_{500}$ . We found that the median scaling factor of  $T_{ap}$  and  $T_{500}$  of the full sample,  $T_{ap}/T_{500}$ , was 1.2, where  $T_{500}$  is the predicted temperature based on the  $L_{500} - T_{500}$  relation by Pratt et al. (2009) using our value for  $L_{500}$ .

Eckmiller et al. (2011) found that the slope of  $L_X - T$  relation of galaxy groups (26 systems,  $L_x \sim 1 - 26 \times 10^{42} \text{ erg s}^{-1}$ ) is slightly shallower than that derived for clusters (HIFLUGCS), but they are still consistent within the errors. These authors found no significant change either of the slope derived from a sample that combined groups and clusters to a sample consisting of clusters only, which is consistent with the results reported by Osmond & Ponman (2004). We found that the slope derived from the current sample (including groups and clusters) agrees well with the slope obtained from clusters only (HIFLUGCS sample), but is lower than the slope of the REXCESS sample.

The current slope of the  $L_X - T$  relation is significantly lower than the one published in paper I,  $3.41 \pm 0.15$ . The redshifts,

temperatures, and luminosities of the previous sample were revised. Using the updated values, we still find a very steep slope of  $3.48 \pm 0.30$ , thus confirming the initial result (the new fit is shown with a dashed line in Figure 23). The much shallower slope found here based on the full sample is clearly due to the inclusion of the new objects, which have a wider temperature and luminosity range. As discussed above, when excluding the low-luminosity systems from the full sample, the slope becomes steep,  $3.07 \pm 0.19$ , which is consistent within  $1.4\sigma$  with the updated slope,  $3.48 \pm 0.30$ , for the paper I-sample.

To estimate the intrinsic scatter in the  $L_X - T$  relation, we followed the method used by Pratt et al. (2009). First we estimated the raw scatter using the error-weighted orthogonal distances to the regression line (Eqs. 3 and 4 in Pratt et al. 2009). Then we computed the intrinsic scatter as the mean value of the quadratic differences between the raw scatters and the statistical errors. The error of the intrinsic scatter was computed as the standard error of its value. The computed intrinsic scatter value of the relation,  $0.48 \pm 0.03$ , is slightly higher than the value of REXCESS sample,  $0.32 \pm 0.06$ .

The updated  $L_X - T$  relation was derived for the first time from a sample comprising 345 clusters drawn from a single survey and spans a wide redshift range ( $0.03 < z < 0.67$ ). Of these, 210 clusters have spectroscopic redshifts for at least one cluster member galaxy. The redshifts and X-ray parameters of the sample are measured in a consistent way. The sample has X-ray spectroscopic temperature measurements from 0.5 to 7.5 keV and a bolometric luminosity range of  $L_{500} \sim 1.0 \times 10^{42} - 1.0 \times 10^{45}$  erg s<sup>-1</sup>.

Based on the SDSS, we were able to identify only about half of our X-ray cluster candidates. The other 50 percent probably represent a more luminous population. The omission of that subsample may have an influence on the  $L_X - T$  relation that is yet to be quantified. However, including luminous distant clusters does not have a significant effect on the slope of the  $L_X - T$  relation (Hilton et al. 2012), as described in the subsequent section. Moreover, the current sample does not include distant clusters beyond  $z = 0.7$ , therefore we defer measuring the evolution of the normalisation of the  $L_X - T$  relation to a future study.

#### 4.4.2. Evolution of the slope and intrinsic scatter

Based on the first data release of the XCS, Hilton et al. (2012) investigated a possible evolution of the slope and intrinsic scatter of the  $L_X - T$  relation in three redshift bins. A sample of 211 clusters with spectroscopic redshift up to 1.5 was used for this exercise. No evidence for evolution in either the slope or intrinsic scatter as a function of redshift was found.

Using our much larger sample of clusters with measured X-ray spectroscopic parameters, we also investigated a possible evolution of the mentioned parameters of the  $L_X - T$  relation. We divided our sample into three subsamples with redshift bins similar to those used by Hilton et al. (2012),  $0.03 \leq z < 0.25$ ,  $0.25 \leq z < 0.5$ , and  $0.5 \leq z < 0.7$ . The numbers of clusters per redshift bin are listed in Table 3. Our two low-redshift subsamples are about twice as large as the XCS corresponding subsamples. The number of clusters in the high-redshift bin are similar, but the XCS comprises clusters up to redshift 1.5. In general, there are about 75 cluster in common between our sample and the XCS-DR1 sample that were used to derive the  $L_X - T$  relation. Of these clusters in common, 44 systems were published from our survey in paper I.

The  $L_X - T$  relations of our subsamples are shown in Figure 24. When we fitted these subsamples using the BCES orthogonal regression method, we found that the relation slope of the subsamples in the intermediate- and high-redshift bins are consistent, while the subsample in the lowest redshift bin has a shallower slope. The reason is that the low-redshift subsample includes groups/clusters with low temperature and luminosity, which produces a shallower slope. Moreover, the present slope of the low-redshift subsample is lower than the published one of the corresponding XCS-DR1 subsample and those of the REXCESS and HIFLUGCS samples. On the other hand, the slopes of the intermediate- and high-redshift subsamples agree with the slopes of the corresponding XCS-DR1 subsamples. The intrinsic scatter of all subsamples agree with each other. Table 3 also lists the fitted parameters (intercept and slope) of the  $L_X - T$  relations and their intrinsic scatter together with published values (slope, sample size, reference).

When we fit the  $L_X - T$  for the low-redshift subsample after excluding the groups with low luminosity (i.e.  $L_{500} < 5 \times 10^{42}$  erg s<sup>-1</sup>), the slope of the relation becomes  $2.86 \pm 0.41$ , which agrees with the intermediate- and high-redshift subsamples as well as with the corresponding published slopes given in Table 3. We

thus confirm the finding by Hilton et al. (2012) that the  $L_X - T$  relation does not show a significant change of its slope and its intrinsic scatter as a function of redshift.

#### 4.5. Distribution of the luminosity with redshift

Figure 25 shows the distribution of the bolometric luminosity  $L_{500}$  as a function of the redshift for all 530 clusters with redshifts that were determined in the present work. Included are also the 1730 systems from the MCXC catalogue below redshift 0.8. The X-ray luminosity  $L_{500}$  in 0.1 – 2.4 keV of the MCXC sample was converted into the bolometric luminosity  $L_{500}$  by assuming the factor  $L_{\text{bol}, 500}/L_{\text{band}, 500} = 1.3$ . This factor was derived as the median of  $L_{\text{bol}, 500}/L_{\text{band}, 500}$  for the 23 systems in common between the cluster sample with reliable parameters from the spectral fitting and MCXC catalogue.

It is obvious that our X-ray-selected samples extend to include groups and clusters with low luminosity. The sensitivity of XMM-Newton and deeper exposures for some fields allow us to detect less-luminous clusters over the redshift range, as shown in Figure 25.

## 5. Summary and outlook

We have presented the optically confirmed cluster sample of 530 galaxy groups and clusters from the 2XMMi/SDSS Galaxy Cluster Survey. The survey consists of 1180 X-ray cluster candidates with at least 80 net photon counts selected from the second XMM-Newton serendipitous source catalogue (2XMMi-DR3) that are located in the footprint of the SDSS-DR7. The survey area is 210 deg<sup>2</sup> considering the XMM-Newton field of view has a radius of 15 arcmin. We developed a finding algorithm for detecting the optical counterparts of the X-ray cluster candidates and for constraining their redshifts using the photometric and, where available, the spectroscopic redshifts of the surrounding galaxies from the SDSS-DR8 data. A cluster was recognized when there were at least eight member galaxies within a radius of 560 kpc from the X-ray emission peak with photometric redshift in the redshift interval of the redshift of the likely identified BCG,  $z_{\text{p, BCG}} \pm 0.04(1 + z_{\text{p, BCG}})$ . The BCG was identified as the brightest galaxy among those galaxies within one arcmin from the X-ray position that show a peak in the histogram of their photometric redshifts.

The cluster photometric and spectroscopic redshift was measured as the weighted average of the photometric and the available spectroscopic redshifts, respectively, of the cluster galaxies within 560 kpc from the X-ray position. The measured redshifts agree well with the available redshifts in the literature; to date, 301 clusters are known as optically selected clusters with redshift measurements. Moreover, 310 clusters of the optically confirmed cluster sample have spectroscopic redshifts for at least one cluster member. The measured photometric redshifts agree well with the measured spectroscopic ones from the survey. The cluster redshifts of the optically confirmed cluster sample span a wide redshift range from 0.03 to 0.70. We reduced and analysed the X-ray data of this sample in an automated way to compute their X-ray properties.

We presented a cluster catalogue from the survey comprising 345 X-ray-selected groups and clusters with their X-ray parameters derived from the spectral fits including the published sample in paper I. In addition to the best-fitting parameters, we estimated the physical properties ( $R_{500}$ ,  $L_{500}$  and  $M_{500}$ ) of this sample from an iterative procedure based on published scaling

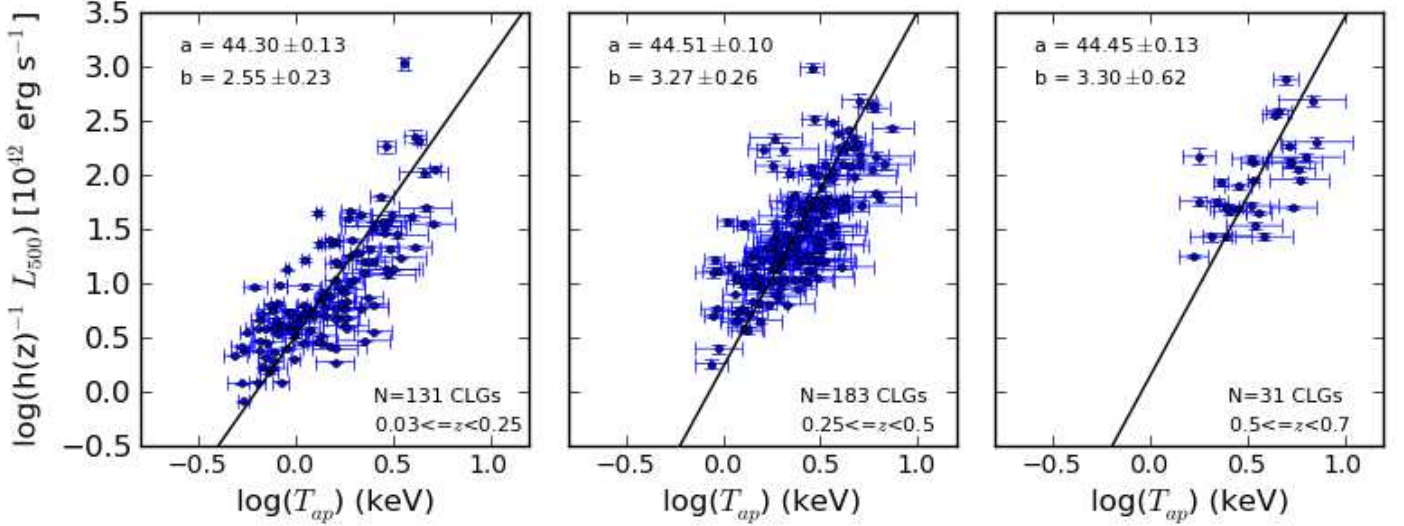


**Fig. 24.**  $L_{500} - T_{ap}$  relations for the three subsamples in redshift bins. The redshift bin and the cluster number of these subsamples are written in the lower right of the figure. The best-fit line of the subsamples is presented by the solid line, while their parameters (intercepts,  $a$ , and slopes,  $b$ ) are written in the upper left corner.

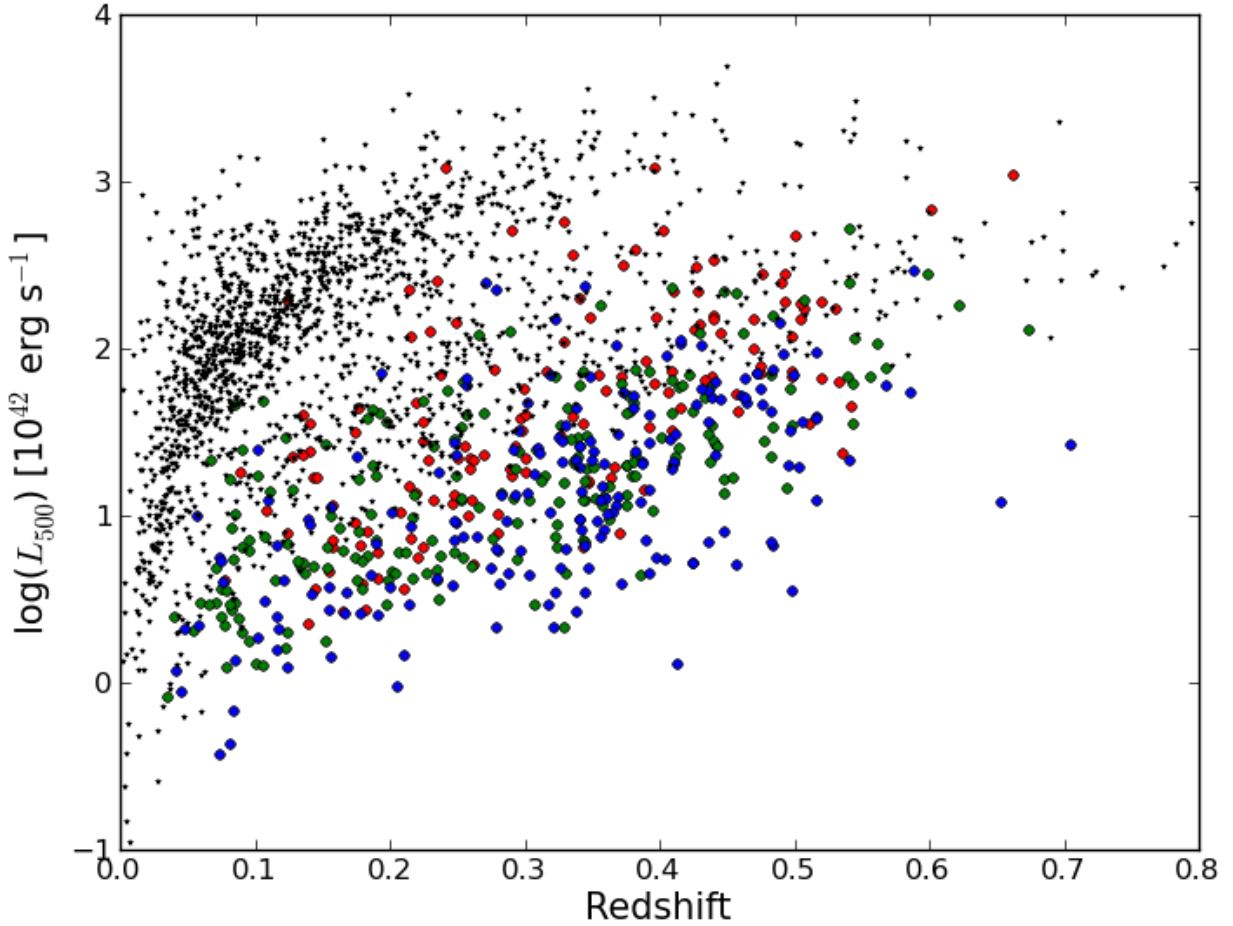


**Fig. 25.** Distribution of the estimated bolometric luminosity,  $L_{500}$ , as a function of the redshift for the first (red dots) and extended (green dots) cluster sample with X-ray spectroscopic parameters, the cluster sample (blue dots) with X-ray parameters based on the given flux in the 2XMMi-DR3 catalogue, and the MCXC cluster sample (black stars) (Piffaretti et al. 2011).

**Table 3.** Fit parameters of the  $L_{500} - T_{ap}$  relation, derived from the BCES orthogonal regression method, for the three subsamples in redshift bins. The fitted model is  $\log(h(z)^{-1} L_{500}) = a + b \log(T_{ap}/5)$ , and the fit parameters (a and b) are also shown in the legend of Figure 24.

redshift range	$N_{CLGs}$	intercept	current slope	$\sigma_{\log L_{500}}$	published slope	$N_{CLGs, pub.}$	ref.
$0.03 \leq z < 0.25$	131	$44.30 \pm 0.13$	$2.55 \pm 0.23$	$0.45 \pm 0.04$	$3.18 \pm 0.22$	96	1
					$3.35 \pm 0.32$	31	2
					$2.94 \pm 0.16$	64	3
$0.25 \leq z < 0.50$	183	$44.51 \pm 0.10$	$3.27 \pm 0.26$	$0.49 \pm 0.04$	$2.82 \pm 0.25$	77	1
$0.50 \leq z < 0.70$	31	$44.45 \pm 0.13$	$3.30 \pm 0.62$	$0.41 \pm 0.07$	$2.89 \pm 0.45$	38	1

**References.** 1- Hilton et al. (2012); 2- Pratt et al. (2009); 3- Mittal et al. (2011).

relations. We investigated the  $L_X - T$  relations for the first time based on a large cluster sample with X-ray spectroscopic parameters drawn from a single survey. The current sample includes groups and clusters with wide ranges of temperatures and luminosities. The slope of the relation is consistent with the published ones of clusters with high temperatures and luminosities. After excluding the low-luminosity groups, we found no significant change of the slope and the intrinsic scatter of the relation with redshift when dividing the sample into three redshift bins. When including the low-luminosity groups in the low-redshift subsample, the slope was no longer consistent with the intermediate- and high-redshift subsamples.

In addition to the cluster sample with X-ray spectroscopic data, we presented the remainder of the optically confirmed cluster sample with their X-ray parameters based on the given flux in the 2XMMi-DR3 catalogue. We used the 2XMMi-DR3 flux because of their low-quality X-ray data, which are insufficient to perform spectral fitting. This sample comprises 185 groups and clusters with fluxes and luminosity in the energy band 0.5-2.0 keV and physical parameters ( $R_{500}$ ,  $L_{500}$ ,  $M_{500}$ , and  $T_{500}$ ).

This is the largest X-ray-selected cluster catalogue to date based on XMM-Newton observations. It comprises 530 clusters with optical and X-ray properties, spanning the redshift range  $0.03 < z < 0.70$ . More than 75 percent of the cluster sample are newly discovered clusters in X-ray wavelengths. About 40 percent of the sample are systems new to the literature according to current entries in the NED.

In the future we plan to study the remainder of the X-ray cluster candidates that were not detected by the current detection algorithm. They are either poor or at high redshifts. For the distant clusters, we plan follow-up by imaging and spectroscopy. For the X-ray cluster candidates with galaxies detected in SDSS imaging and have not been validated by the current algorithm, we plan to improve the current algorithm to constrain their redshifts. The new sample from the survey, especially the distant ones, will allow us to investigate the evolution of  $L_X - T$  relation and X-ray-optical relations.

*Acknowledgements.* This project is supported by the Egyptian Ministry of Higher Education and Scientific Research (MHESR) in cooperation with the Leibniz-Institut für Astrophysik Potsdam (AIP), Germany. We acknowledge the partial support by the Deutsches Zentrum für Luft- und Raumfahrt (DLR) under contract number 50 QR 0802. We also acknowledge financial support from the ARCHES project (7th Framework of the European Union, n° 313146). We thank the referee for the valuable comments that helped to improve the paper. The XMM-Newton project is an ESA Science Mission with instruments and contributions directly funded by ESA Member States and the USA (NASA). This research has made use of the NASA/IPAC Extragalactic Database (NED) which is operated by the Jet Propulsion Laboratory, California Institute of Technology, under contract with the National Aeronautics and Space Administration (NASA). Funding for SDSS-III has been provided by the Alfred P. Sloan Foundation, the Participating Institutions, the National Science Foundation, and the U.S. Department of Energy. The SDSS-III web site is <http://www.sdss3.org/>. SDSS-III is managed by the Astrophysical Research Consortium for the

Participating Institutions of the SDSS-III Collaboration including the University of Arizona, the Brazilian Participation Group, Brookhaven National Laboratory, University of Cambridge, University of Florida, the French Participation Group, the German Participation Group, the Instituto de Astrofísica de Canarias, the Michigan State/Notre Dame/JINA Participation Group, Johns Hopkins University, Lawrence Berkeley National Laboratory, Max Planck Institute for Astrophysics, New Mexico State University, New York University, Ohio State University, Pennsylvania State University, University of Portsmouth, Princeton University, the Spanish Participation Group, University of Tokyo, University of Utah, Vanderbilt University, University of Virginia, University of Washington, and Yale University.

## References

- Adami, C., Mazure, A., Pierre, M., et al. 2011, *A&A*, 526, A18  
Akritas, M. G. & Bershady, M. A. 1996, *ApJ*, 470, 706  
Allen, S. W., Evrard, A. E., & Mantz, A. B. 2011, *ARA&A*, 49, 409  
Arnaud, K. A. 1996, in *Astronomical Society of the Pacific Conference Series*, Vol. 101, *Astronomical Data Analysis Software and Systems V*, ed. G. H. Jacoby & J. Barnes, 17  
Arnaud, M., Pratt, G. W., Piffaretti, R., et al. 2010, *A&A*, 517, A92  
Arviset, C., Guainazzi, M., Hernandez, J., et al. 2002, *ArXiv Astrophysics e-prints*  
Bahcall, N. A., McKay, T. A., Annis, J., et al. 2003, *ApJS*, 148, 243  
Barkhouse, W. A., Green, P. J., Vikhlinin, A., et al. 2006, *ApJ*, 645, 955  
Berlind, A. A., Frieman, J., Weinberg, D. H., et al. 2006, *ApJS*, 167, 1  
Blanton, E. L., Randall, S. W., Clarke, T. E., et al. 2011, *ApJ*, 737, 99  
Böhlinger, H., Collins, C. A., Guzzo, L., et al. 2002, *ApJ*, 566, 93  
Böhlinger, H., Schuecker, P., Guzzo, L., et al. 2004, *A&A*, 425, 367  
Böhlinger, H., Voges, W., Huchra, J. P., et al. 2000, *ApJS*, 129, 435  
Borgani, S., Rosati, P., Tozzi, P., et al. 2001, *ApJ*, 561, 13  
Boschin, W. 2002, *A&A*, 396, 397  
Burenin, R. A., Vikhlinin, A., Hornstrup, A., et al. 2007, *ApJS*, 172, 561  
Carlberg, R. G., Yee, H. K. C., Morris, S. L., et al. 2001, *ApJ*, 552, 427  
Clerc, N., Sadibekova, T., Pierre, M., et al. 2012, *MNRAS*, 3120  
de Hoon, A., Lamer, G., Schwope, A., et al. 2013, *A&A*, 551, A8  
dell’Antonio, I. P., Geller, M. J., & Fabricant, D. G. 1994, *AJ*, 107, 427  
Dietrich, J. P., Erben, T., Lamer, G., et al. 2007, *A&A*, 470, 821  
Eckmiller, H. J., Hudson, D. S., & Reiprich, T. H. 2011, *A&A*, 535, A105  
Evans, I. N., Primi, F. A., Glotfelty, K. J., et al. 2010, *ApJS*, 189, 37  
Falco, E. E., Kurtz, M. J., Geller, M. J., et al. 1999, *PASP*, 111, 438  
Fassbender, R., Böhlinger, H., Nastasi, A., et al. 2011, *New Journal of Physics*, 13, 125014  
Finoguenov, A., Connelly, J. L., Parker, L. C., et al. 2009, *ApJ*, 704, 564  
Finoguenov, A., Guzzo, L., Hasinger, G., et al. 2007, *ApJS*, 172, 182  
Finoguenov, A., Watson, M. G., Tanaka, M., et al. 2010, *MNRAS*, 403, 2063  
Forman, W., Jones, C., Cominsky, L., et al. 1978, *ApJS*, 38, 357  
Gal, R. R., de Carvalho, R. R., Lopes, P. A. A., et al. 2003, *AJ*, 125, 2064  
Gladders, M. D. & Yee, H. K. C. 2005, *ApJS*, 157, 1  
Goto, T., Sekiguchi, M., Nichol, R. C., et al. 2002, *AJ*, 123, 1807  
Grove, L. F., Benoist, C., & Martel, F. 2009, *A&A*, 494, 845  
GUNN, J. E., HOESSEL, J. G., & OKE, J. B. 1986, *ApJ*, 306, 30  
Hao, J., McKay, T. A., Koester, B. P., et al. 2010, *ApJS*, 191, 254  
Hilton, M., Romer, A. K., Kay, S. T., et al. 2012, *MNRAS*, 3303  
Horner, D. J., Perlman, E. S., Ebeling, H., et al. 2008, *ApJS*, 176, 374  
Hughes, J. P. & Birkinshaw, M. 1998, *ApJ*, 497, 645  
Kalberla, P. M. W., Burton, W. B., Hartmann, D., et al. 2005, *A&A*, 440, 775  
Knobel, C., Lilly, S. J., Iovino, A., et al. 2009, *ApJ*, 697, 1842  
Koester, B. P., McKay, T. A., Annis, J., et al. 2007, *ApJ*, 660, 239  
Kolokotronis, V., Georgakakis, A., Basilakos, S., et al. 2006, *MNRAS*, 366, 163  
Krumpe, M., Lamer, G., Corral, A., et al. 2008, *A&A*, 483, 415

- Lloyd-Davies, E. J., Romer, A. K., Mehrrens, N., et al. 2011, *MNRAS*, 418, 14
- Lopes, P. A. A., de Carvalho, R. R., Gal, R. R., et al. 2004, *AJ*, 128, 1017
- Markevitch, M. 1998, *ApJ*, 504, 27
- Maughan, B. J., Giles, P. A., Randall, S. W., Jones, C., & Forman, W. R. 2012, *MNRAS*, 421, 1583
- McConnachie, A. W., Patton, D. R., Ellison, S. L., & Simard, L. 2009, *MNRAS*, 395, 255
- McDowell, J. C., Clements, D. L., Lamb, S. A., et al. 2003, *ApJ*, 591, 154
- Mehrtens, N., Romer, A. K., Hilton, M., et al. 2012, *MNRAS*, 2912
- Merchán, M. E. & Zandivarez, A. 2005, *ApJ*, 630, 759
- Mewe, R., Lemen, J. R., & van den Oord, G. H. J. 1986, *A&AS*, 65, 511
- Mittal, R., Hicks, A., Reiprich, T. H., & Jaritz, V. 2011, *A&A*, 532, A133
- Mühlegger, M. 2010, PhD thesis, Technische Universität München
- Mullis, C. R., McNamara, B. R., Quintana, H., et al. 2003, *ApJ*, 594, 154
- Olsen, L. F., Benoist, C., Cappi, A., et al. 2007, *A&A*, 461, 81
- Osmond, J. P. F. & Ponman, T. J. 2004, *MNRAS*, 350, 1511
- Piffaretti, R., Arnaud, M., Pratt, G. W., Pointecouteau, E., & Melin, J.-B. 2011, *A&A*, 534, A109
- Plionis, M., Basilakos, S., Georgantopoulos, I., & Georgakakis, A. 2005, *ApJ*, 622, L17
- Postman, M., Lauer, T. R., Oegerle, W., & Donahue, M. 2002, *ApJ*, 579, 93
- Pratt, G. W., Arnaud, M., Piffaretti, R., et al. 2010, *A&A*, 511, A85
- Pratt, G. W., Croston, J. H., Arnaud, M., & Böhringer, H. 2009, *A&A*, 498, 361
- Ramella, M., Boschin, W., Fadda, D., & Nonino, M. 2001, *A&A*, 368, 776
- Reichert, A., Böhringer, H., Fassbender, R., & Mühlegger, M. 2011, *A&A*, 535, A4
- Reiprich, T. H. & Böhringer, H. 2002, *ApJ*, 567, 716
- Romer, A. K., Collins, C. A., Böhringer, H., et al. 1994, *Nature*, 372, 75
- Romer, A. K., Nichol, R. C., Holden, B. P., et al. 2000, *ApJS*, 126, 209
- Romer, A. K., Viana, P. T. P., Liddle, A. R., & Mann, R. G. 2001, *ApJ*, 547, 594
- Rosati, P., Borgani, S., & Norman, C. 2002, *ARA&A*, 40, 539
- Rykoff, E. S., McKay, T. A., Becker, M. R., et al. 2008, *ApJ*, 675, 1106
- Sarazin, C. L. 1988, *X-ray emission from clusters of galaxies* (Cambridge, UK: Cambridge Univ. Press)
- Scharf, C. A., Jones, L. R., Ebeling, H., et al. 1997, *ApJ*, 477, 79
- Schuecker, P., Böhringer, H., Collins, C. A., & Guzzo, L. 2003, *A&A*, 398, 867
- Schuecker, P., Böhringer, H., & Voges, W. 2004, *A&A*, 420, 61
- Sehgal, N., Hughes, J. P., Wittman, D., et al. 2008, *ApJ*, 673, 163
- Sunyaev, R. A. & Zeldovich, I. B. 1980, *ARA&A*, 18, 537
- Sunyaev, R. A. & Zeldovich, Y. B. 1972, *Comments on Astrophysics and Space Physics*, 4, 173
- Szabo, T., Pierpaoli, E., Dong, F., Pipino, A., & Gunn, J. 2011, *ApJ*, 736, 21
- Takey, A., Schwobe, A., & Lamer, G. 2011, *A&A*, 534, A120
- Tundo, E., Moretti, A., Tozzi, P., et al. 2012, *A&A*, 547, A57
- Vikhlinin, A., Burenin, R. A., Ebeling, H., et al. 2009, *ApJ*, 692, 1033
- Vikhlinin, A., McNamara, B. R., Forman, W., et al. 1998, *ApJ*, 502, 558
- Voit, G. M. 2005, *Reviews of Modern Physics*, 77, 207
- Watson, M. G., Schröder, A. C., Fyfe, D., et al. 2009, *A&A*, 493, 339
- Wen, Z. L., Han, J. L., & Liu, F. S. 2009, *ApJS*, 183, 197
- White, R. A., Bliton, M., Bhavsar, S. P., et al. 1999, *AJ*, 118, 2014
- Wilms, J., Allen, A., & McCray, R. 2000, *ApJ*, 542, 914
- Wittman, D., Dell'Antonio, I. P., Hughes, J. P., et al. 2006, *ApJ*, 643, 128
- Yoon, J. H., Schawinski, K., Sheen, Y.-K., Ree, C. H., & Yi, S. K. 2008, *ApJS*, 176, 414
- Zwicky, F., Herzog, E., & Wild, P. 1961, *Pasadena: California Institute of Technology*, volume I



**Table 1.** First ten entries of the X-ray-selected group/cluster sample (345 objects) from the 2XMMi/SDSS Galaxy Cluster Survey with X-ray parameters from the spectral fitting.

detid <sup>a</sup>	Name <sup>a</sup> IAUNAME	ra <sup>a</sup> (deg)	dec <sup>a</sup> (deg)	obsid <sup>a</sup>	z <sup>b</sup>	scale kpc''	R <sub>ap</sub> (kpc)	R <sub>500</sub> (kpc)	T <sub>ap</sub> (keV)	+eT <sub>ap</sub> (keV)	-eT <sub>ap</sub> (keV)	F <sub>ap</sub> <sup>c</sup>	+eF <sub>ap</sub>	-eF <sub>ap</sub>	L <sub>ap</sub> <sup>d</sup>	+eL <sub>ap</sub>	-eL <sub>ap</sub>
(1)	(2)	(3)	(4)	(5)	(6)	(7)	(8)	(9)	(10)	(11)	(12)	(13)	(14)	(15)	(16)	(17)	(18)
002294	2XMM J001817.2+161740	4.57190	16.29470	0111000101	0.5401	6.35	476.50	810.94	4.57	0.78	0.60	16.74	0.58	0.79	144.72	5.58	5.52
004444	2XMM J003318.4-212447	8.32687	-21.41319	0044350101	0.1897	3.17	161.44	579.22	2.25	0.66	0.40	3.75	0.28	0.27	3.66	0.19	0.21
005825	2XMM J003917.9+004200	9.82489	0.70013	0203690101	0.2801	4.24	152.81	483.64	1.43	0.77	0.29	0.88	0.06	0.06	2.10	0.13	0.17
005842	2XMM J003922.4+004809	9.84343	0.80269	0203690101	0.4145	5.49	395.23	618.80	4.02	0.64	0.52	3.55	0.08	0.08	18.33	0.44	0.48
005901	2XMM J003942.2+004533	9.92584	0.75919	0203690101	0.4156	5.50	247.44	589.18	2.35	0.43	0.33	2.51	0.12	0.08	14.02	0.67	0.55
006070	2XMM J004039.2+253106	10.16344	25.51840	0153030101	0.1517	2.64	142.48	632.85	1.51	0.13	0.10	10.55	0.49	0.41	6.37	0.33	0.22
006469	2XMM J004156.8+253151	10.48690	25.53105	0153030101	0.1278	2.28	150.73	579.30	3.18	1.09	0.77	5.21	0.19	0.34	2.10	0.10	0.09
006920	2XMM J004231.2+005114	10.63008	0.85401	0090070201	0.1579	2.73	114.55	501.99	2.16	0.92	0.47	1.37	0.10	0.09	0.89	0.07	0.04
007340	2XMM J004252.6+004259	10.71952	0.71650	0090070201	0.2697	4.13	421.41	579.12	3.12	0.90	0.61	4.14	0.19	0.15	8.45	0.44	0.34
007362	2XMM J004253.7-093423	10.72397	-9.57311	0065140201	0.4069	5.43	260.60	613.30	3.29	1.25	0.74	3.03	0.20	0.24	15.14	1.16	0.94

**Table 1.** continued.

detid <sup>a</sup>	L <sub>500</sub> <sup>e</sup>	±eL <sub>500</sub>	M <sub>500</sub> <sup>f</sup>	±eM <sub>500</sub>	nH <sup>g</sup>	objid <sup>h</sup> (BCG)	RA <sup>h</sup> (deg)	Dec <sup>h</sup> (deg)	z <sub>p</sub> <sup>h</sup>	z <sub>s</sub> <sup>h</sup>	N <sub>zs</sub> <sup>h</sup>	z <sub>type</sub> <sup>h</sup>	offset <sup>h</sup> (kpc)	NED-Name	ref.
(1)	(19)	(20)	(21)	(22)	(23)	(24)	(25)	(26)	(27)	(28)	(29)	(30)	(31)	(32)	(33)
002294	521.28	31.45	27.28	5.24	0.0393	1237679454926995783	4.57107	16.29433	0.5401	0.0000	0	photo-z	20.49	RX J0018.2+1617	1,2
004444	17.49	0.71	6.67	1.35	0.0153	1237673016766496932	8.32630	-21.41445	0.1897	0.0000	0	photo-z	17.22	-	-
005825	7.80	0.28	4.28	0.91	0.0198	1237663204918493337	9.82501	0.69981	0.2710	0.2801	1	spec-z	5.14	SDSS CE J009.833157+00.701518	3,4,5
005842	59.67	2.50	10.46	2.03	0.0197	1237663204918493446	9.84605	0.79222	0.3945	0.4145	3	spec-z	213.01	-	-
005901	44.13	2.10	9.04	1.78	0.0195	1237663204918493223	9.92730	0.76163	0.3988	0.4156	2	spec-z	56.24	WHL J003942.5+004541	5,6
006070	26.71	1.08	8.36	1.65	0.0368	1237678580906524886	10.16314	25.51779	0.1517	0.0000	0	photo-z	6.62	-	-
006469	14.21	0.07	6.26	1.27	0.0384	1237680071245365404	10.48821	25.52932	0.1278	0.0000	0	photo-z	18.10	-	-
006920	6.43	0.06	4.20	0.89	0.0179	1237663716555882709	10.63094	0.85020	0.1526	0.1579	4	spec-z	36.87	GMBCG J010.63096+00.85021	4,6
007340	23.13	1.33	7.27	1.46	0.0178	1237663204918886547	10.71962	0.71844	0.2604	0.2697	4	spec-z	28.79	SDSS CE J010.717058+00.725393	3,5,7
007362	54.86	4.07	10.09	1.99	0.0270	1237652947993428384	10.72131	-9.57365	0.4069	0.0000	0	photo-z	52.83	GMBCG J010.72131-09.57365	5,6

**Notes.** The full catalogue is available at CDS. <sup>(a)</sup> All these parameters are extracted from the 2XMMi-DR3 catalogue. <sup>(b)</sup> The cluster redshift is from col. (28) otherwise from col. (27). <sup>(c)</sup> Aperture X-ray flux  $F_{\text{ap}}$  [0.5-2.0] keV and its positive and negative errors in units of  $10^{-14}$  erg cm<sup>-2</sup> s<sup>-1</sup>. <sup>(d)</sup> Aperture X-ray luminosity  $L_{\text{ap}}$  [0.5-2.0] keV and its positive and negative errors in units of  $10^{42}$  erg s<sup>-1</sup>. <sup>(e)</sup> X-ray bolometric luminosity  $L_{500}$  and its error in units of  $10^{42}$  erg s<sup>-1</sup>. <sup>(f)</sup> The cluster mass  $M_{500}$  and its error in units of  $10^{13}$  M<sub>⊙</sub>. <sup>(g)</sup> The Galactic HI column in units  $10^{22}$  cm<sup>-2</sup>. <sup>(h)</sup> These parameters are obtained from the developed optical detection algorithm.

**References.** 1- Romer et al. (2000); 2- Kolokotronis et al. (2006); 3- Goto et al. (2002); 4- Koester et al. (2007); 5- Wen et al. (2009); 6- Hao et al. (2010); 7- Plionis et al. (2005); 8- Merchán & Zandivarez (2005); 9- Bahcall et al. (2003); 10- Vikhlinin et al. (1998); 11- Mullis et al. (2003); 12- Gal et al. (2003); 13- Burenin et al. (2007); 14- Horner et al. (2008); 15- Finoguenov et al. (2007); 16- McConnachie et al. (2009); 17- Olsen et al. (2007); 18- Grove et al. (2009); 19- Falco et al. (1999); 20- Ramella et al. (2001); 21- Zwicky et al. (1961); 22- dell'Antonio et al. (1994); 23- Berlind et al. (2006); 24- Dietrich et al. (2007); 25- GUNN et al. (1986); 26- Gladders & Yee (2005); 27- Barkhouse et al. (2006); 28- McDowell et al. (2003); 29- Schuecker et al. (2004); 30- Wittman et al. (2006); 31- Carlberg et al. (2001); 32- Finoguenov et al. (2009); 33- Hughes & Birkinshaw (1998); 34- Sehgal et al. (2008); 35- Postman et al. (2002).

**Table 2.** First ten entries of the X-ray-selected group/cluster sample (185 systems) from the 2XMMi/SDSS Galaxy Cluster Survey with X-ray parameters based on the given flux in the 2XMMi-DR3 catalogue.

detid <sup>a</sup>	Name <sup>a</sup> IAUNAME	ra <sup>a</sup> (deg)	dec <sup>a</sup> (deg)	obsid <sup>a</sup>	z <sup>b</sup>	scale kpc/''	R <sub>500</sub> (kpc)	F <sub>cat</sub> <sup>a,c</sup>	±eF <sub>cat</sub>	L <sub>cat</sub> <sup>d</sup>	±eL <sub>cat</sub>	L <sub>500</sub> <sup>e</sup>	±eL <sub>500</sub>	M <sub>500</sub> <sup>f</sup>	±eM <sub>500</sub>	T <sub>500</sub> (keV)	±eT <sub>500</sub> (keV)
(1)	(2)	(3)	(4)	(5)	(6)	(7)	(8)	(9)	(10)	(11)	(12)	(13)	(14)	(15)	(16)	(17)	(18)
006511	2XMM J004205.5-093613	10.52296	-9.60375	0065140201	0.3256	4.71	582.39	3.30	0.47	11.51	1.63	29.35	4.66	7.87	1.67	1.84	0.45
007481	2XMM J004259.7-092634	10.74900	-9.44286	0065140201	0.4151	5.49	678.59	7.97	1.21	49.11	7.44	106.34	20.98	13.80	2.93	2.65	0.63
011071	2XMM J005608.0+004103	14.03365	0.68427	0303110401	0.4607	5.84	588.27	2.71	0.60	21.40	4.74	51.85	13.25	9.48	2.18	2.12	0.53
014038	2XMM J010606.8+004926	16.52863	0.82407	0150870201	0.2564	3.98	680.44	13.69	1.54	27.55	3.11	60.33	7.82	11.62	2.34	2.30	0.55
014050	2XMM J010610.0+005110	16.54201	0.85302	0150870201	0.2566	3.99	689.89	15.44	1.42	31.12	2.86	65.80	7.60	12.12	2.41	2.36	0.56
021043	2XMM J015558.5+053159	28.99394	5.53329	0153030701	0.4312	5.62	671.20	5.82	0.85	39.27	5.76	105.58	20.88	13.61	2.90	2.64	0.63
021688	2XMM J020056.5-092119	30.23615	-9.35526	0203840201	0.3381	4.83	549.44	2.29	0.24	8.72	0.92	21.37	2.51	6.70	1.40	1.67	0.41
023255	2XMM J021447.5-005425	33.69817	-0.90720	0201020201	0.2650	4.08	484.82	0.88	0.12	1.91	0.27	7.50	0.78	4.24	0.93	1.23	0.32
030889	2XMM J023458.7-085055	38.74463	-8.84868	0150470601	0.2484	3.89	603.14	4.15	0.53	7.77	1.00	27.63	4.52	8.02	1.70	1.83	0.45
033092	2XMM J024810.2+311511	42.04268	31.25311	0111490401	0.3871	5.27	532.12	2.17	0.39	11.31	2.03	20.99	4.49	6.44	1.46	1.64	0.42
034341	2XMM J030212.0+001108	45.55036	0.18583	0041170101	0.6523	6.94	413.91	0.43	0.08	7.91	1.49	12.12	2.98	4.15	1.01	1.33	0.35

**Table 2.** continued.

detid <sup>a</sup>	objid <sup>g</sup> (BCG)	RA <sup>g</sup> (deg)	DEC <sup>g</sup> (deg)	$\bar{z}_p$ <sup>g</sup>	$\bar{z}_s$ <sup>g</sup>	N <sub>zs</sub> <sup>g</sup>	z <sub>type</sub> <sup>g</sup>	offset <sup>g</sup> (kpc)	NED-Name	ref.
(1)	(19)	(20)	(21)	(22)	(23)	(24)	(25)	(26)	(27)	(28)
006511	1237652947993297563	10.51514	-9.60060	0.3256	0.0000	0	photo-z	138.56	-	-
007481	1237652630713795354	10.75138	-9.43350	0.4151	0.0000	0	photo-z	191.29	CXO J004259.9-092704	1
011071	1237663204920328298	14.04250	0.68188	0.4607	0.0000	0	photo-z	192.67	-	-
014038	1237663204921376994	16.52926	0.81949	0.2515	0.2564	4	spec-z	68.21	SDSS CE J016.528793+00.817471	2,3,4,5,6
014050	1237663785278374092	16.54324	0.85569	0.2492	0.2566	5	spec-z	42.90	MaxBCG J016.54324+00.85569	4,7,8
021043	1237678663047250389	28.98754	5.53073	0.4312	0.0000	0	photo-z	143.57	-	-
021688	1237652900224303421	30.23274	-9.35660	0.3472	0.3381	1	spec-z	62.93	-	-
023255	1237680000377684204	33.69949	-0.90894	0.2649	0.2650	1	spec-z	32.01	-	-
030889	1237653500970270877	38.74547	-8.84926	0.2484	0.0000	0	photo-z	13.80	-	-
033092	1237670458043073373	42.04490	31.25411	0.3871	0.0000	0	photo-z	39.90	-	-
034341	1237663784217346252	45.54822	0.18751	0.6516	0.6523	1	spec-z	67.99	BLOX J0302.2+0010.5	9

**Notes.** The full catalogue is available at CDS and contains the information given in columns (1)-(28) in Table 2. <sup>(a)</sup> All these parameters are extracted from the 2XMMi-DR3 catalogue. <sup>(b)</sup> The cluster redshift is from col. (23) otherwise from col. (22). <sup>(c)</sup> The given flux in the 2XMMi-DR3  $F_{\text{cat}}$  [0.5-2.0] keV and its errors in units of  $10^{-14}$  erg cm<sup>-2</sup> s<sup>-1</sup>. <sup>(d)</sup> The computed X-ray luminosity  $L_{\text{cat}}$  [0.5-2.0] keV and its errors in units of  $10^{42}$  erg s<sup>-1</sup>. <sup>(e)</sup> X-ray bolometric luminosity  $L_{500}$  and its error in units of  $10^{42}$  erg s<sup>-1</sup>. <sup>(f)</sup> The cluster mass  $M_{500}$  and its error in units of  $10^{13}$  M<sub>⊙</sub>. <sup>(g)</sup> These parameters are obtained from our detection algorithm in the optical band.

**References.** 1- Evans et al. (2010); 2- Goto et al. (2002); 3- Lopes et al. (2004); 4- Barkhouse et al. (2006); 5- Wen et al. (2009); 6- Hao et al. (2010); 7- Koester et al. (2007); 8- Bahcall et al. (2003); 9- Dietrich et al. (2007); 10- GUNN et al. (1986); 11- Knobel et al. (2009); 12- Olsen et al. (2007); 13- Finoguenov et al. (2007); 14- Gal et al. (2003); 15- McConnachie et al. (2009); 16- Merchán & Zandivarez (2005); 17- Boschin (2002); 18- Kolokotronis et al. (2006); 19- Horner et al. (2008); 20- Zwicky et al. (1961); 21- Falco et al. (1999); 22- Burenin et al. (2007); 23- Yoon et al. (2008); 24- Romer et al. (2000); 25- White et al. (1999).